Cu/ZnO(0001) under oxidating and reducing conditions: A first-principles survey of surface structures

O. Warschkow,[1,*] K. Chuasiripattana,[1] M. J. Lyle,[1] B. Delley,[2] and C. Stampfl[1]
[1]*School of Physics, The University of Sydney, Sydney, New South Wales 2006, Australia*
[2]*Paul-Scherrer-Institut, Villigen CH-5232, Switzerland*
(Received 2 November 2010; revised manuscript received 1 August 2011; published 12 September 2011)

We investigate the stability of Cu-exposed ZnO(0001) surface structures in an oxygen environment using density functional theory and the method of *ab initio* atomistic thermodynamics. A two-dimensional phase diagram is constructed which identifies stable surface structures as a function of the copper and oxygen chemical potentials. Two structures with a $(\sqrt{3} \times \sqrt{3})$R30° unit cell are found to be prominently stable at intermediate oxygen and copper chemical potentials. These phases are characterized by a single adlayer of Cu_4O_3 and $Cu_{12}O_{13}$ stoichiometry on ZnO(0001). We rationalize recent experimental observations in the literature in terms of our results.

DOI: 10.1103/PhysRevB.84.125311 PACS number(s): 68.47.Gh, 68.43.Bc, 82.65.+r

I. INTRODUCTION

The Cu/ZnO surface is a well-known heterogeneous catalyst system for the synthesis of methanol[1–3] and the production of hydrogen fuel via the water-gas-shift (WGS) reaction.[4,5] An atomic scale understanding of how the Cu/ZnO catalyst functions is critical to the development of improved catalysts for the chemical industry and the emergent hydrogen economy. Various ideas and models have been advanced on the respective roles of copper and ZnO in facilitating chemical reactions.[6,7] For instance, ZnO is thought to act as a hydrogen reservoir,[1] Cu-Zn alloys have been proposed to be the active phase for methanol synthesis,[8] or metallic copper clusters are considered to be the active species.[9,10] Despite extensive studies into this surface science system, there remains considerable uncertainty about how copper enhances ZnO-based catalysis.

The growth of copper on polar ZnO surfaces was initially studied by various authors[11–16] using x-ray photoelectron spectroscopy (XPS), low-energy ion-scattering spectroscopy (LEIS), and low-energy electron diffraction (LEED) experiments. These studies conclude that copper atoms form into islands of Cu(111) that are of monolayer thickness at low coverage and become three-dimensional at higher coverage. This view is refuted by later scanning tunneling microscopy (STM) experiments[17–19] finding that copper already forms three-dimensional islands at low coverages. The response of such copper deposits to oxidation was also studied by several groups.[16–18,20,21] Dulub *et al.*[18] observe in LEED experiments the formation of a distinct $(\sqrt{3} \times \sqrt{3})$R30° reconstruction when Cu deposits are annealed to 650 K in an oxygen-containing environment. Lazcano *et al.*[20] used XPS to study the binding of oxygen on the Cu/ZnO(0001) surface, reporting a partially oxidized copper layer at the interface between ZnO and bulk copper particles. Further copper deposition also leads to CuO and Cu_2O formation. Most recently, Ozawa *et al.*[21] performed LEED, XPS, and angle-resolved photoelectron spectroscopy (ARPES) experiments and conclude that an ordered Cu_2O overlayer with (111) orientation is formed. Several theoretical studies have considered copper binding to the ZnO surface. In a series of papers from the Catlow group,[22–25] a hybrid quantum mechanical/molecular mechanical (QM/MM) cluster model is used to describe copper atoms and small copper clusters on the ZnO(0001) surface. These studies consider copper in various oxidation states and examine the induced changes to the surface electronic structure and atomic geometries. A more recent cluster study[26,27] steps beyond density functional theory and explores the utility of higher-level *ab initio* correlation methods to the problem of Cu atom binding to ZnO(0001). Meyer and Marx[28] report slab-model density functional theory calculations for copper adatoms, monolayers, and thin films on polar ZnO surfaces, including coadsorption with H and OH. Their findings suggest that the binding of copper to the surface depends critically on the occupation of the electronic bands of the polar surfaces. Most recently, Dai *et al.*[29] explored the relative stability of monolayers of oxygen and copper atoms on the ZnO(0001) surface, concluding that copper leads to enhanced oxygen adsorption. Overall, these experimental and theoretical results highlight the importance of the oxidation state to the atomic structure of the Cu/ZnO surface; however, much of the atomic-scale detail of these oxygen-driven surface reconstructions remain unclear.

In this work, we use the formalism of *ab initio* atomistic thermodynamics[30–36] to develop a phase diagram for the ZnO(0001) surface in contact with an oxygen-containing gas phase and a copper reservoir. We survey a large number of possible surface structures and compare their relative stability under a given environment characterized by copper and oxygen chemical potentials. This reveals several regimes in which distinct CuO_x overlayer reconstructions become stable on the ZnO(0001) surface, including two prominent $(\sqrt{3} \times \sqrt{3})$R30° phases of Cu_4O_3 and $Cu_{12}O_{13}$ stoichiometry. We relate our results to recent experimental findings in the literature.

II. METHOD

A. Density functional theory

Self-consistent total energy calculations are performed in the framework of density functional theory (DFT) as implemented in the DMOL[3] software.[37] Electron exchange and correlation are treated in the generalized gradient approximation (GGA) of Perdew, Burke, and Ernzerhof (PBE;

TABLE I. Calculated and experimental values of the structural parameters for bulk ZnO. a and c are the lattice constants and u is the internal parameter.

	GGA-PBE (This work)	GGA-PBE (Ref. 42)	LDA (Ref. 42)	Experiment (Ref. 43)
a (Å)	3.289	3.282	3.193	3.250
c (Å)	5.313	5.291	5.163	5.207
c/a	1.615	1.612	1.617	1.602
u	0.3788	0.3792	0.3783	0.3817

Ref. 38). The electronic eigenfunctions are expanded in terms of a double-numerical plus polarization (DNP) set of localized atomic-orbital-like basis functions. Matrix elements are evaluated by three-dimensional numerical integrations and scalar-relativistic effects are included via corrections as detailed in Ref. 39. All energies reported herein are obtained using spin-polarized DFT. We observe, however, that for the majority of the structures considered, any spin-density supplied with the initial guess is quenched over the course of the self-consistent procedure.[40] In the Results section, we specifically note those structures for which spin polarization is important.

The hexagonal bulk unit cell of ZnO was geometry optimized using a $16 \times 16 \times 16$ Monkhorst-Pack **k**-point mesh.[41] The calculated structural parameters are given in Table I and are found to be in good agreement with other first-principles calculations[42] and experiment.[43]

We represent the ZnO(0001) surface using a three-dimensionally repeated slab model. A thickness of four ZnO double layers is used which represents a good balance between accuracy and computational expense, considering that we survey a very large number of surface structures and a variety of in-plane super cells. We will comment in various places in the text on the effect of slab thickness on certain selected quantities which include adsorption energies and surface free-energy differences. A more general discussion of slab thickness effects for ZnO(0001) can be found in Refs. 42 and 44.

In the surface perpendicular direction we use a unit cell repeat of 35 Å, which leads to a minimum 15-Å vacuum separation between successive slabs. We tested the use of larger vacuum gaps of up to 70 Å thickness and found these to have negligible effects on adsorption energies and free-energy differences. A surface dipole correction was not applied. The surface of interest in this study is the Zn-terminated ZnO(0001) surface, which is polar. The reverse surface of the slab is, out of necessity, oxygen terminated. We follow Ref. 42 and effect an electronic saturation of the oxygen-terminated surface using one monolayer of quasiatoms with a fractional atomic number of 1/2. These quasiatoms cause the O-terminated surface to become a semiconductor, which helps to suppress any long-ranged interference between the zinc- and oxygen-terminated ends of the slab.

All atoms are fully relaxed in our calculations, except for those in the bottom ZnO double layer and the monolayer of quasiatoms. Integrations over the Brillouin zone of the slab are conducted using **k**-point meshes[41] of $16 \times 16 \times 1$ for a (1×1) surface unit cell. Correspondingly smaller grids are used for larger surface super cells.

Atomic structure views are generated using the XCRYSDEN software.[45]

B. Surface thermodynamics

In order to compare the relative stability of surface structures of different elemental compositions, we use the formalism of *ab initio* atomistic thermodynamics.[30–36] This method has been successfully applied to many surface systems, including several of relevance to this work, namely zinc oxide[44,46–49] and copper oxide.[50–53] In this formalism, the thermodynamically preferred surface reconstruction is the one with the lowest surface Gibbs free energy, γ. Because of the polarity of the ZnO(0001) surface, the free energy must be expressed in *relative* terms with respect to a suitable reference, which we take here to be a bulklike relaxed ZnO(0001) termination. The relative surface free energy is calculated as

$$\Delta\gamma = \frac{1}{A}[\Delta G_{\text{slab}} - \Delta N_{\text{O}}\mu_{\text{O}} - \Delta N_{\text{Zn}}\mu_{\text{Zn}} - N_{\text{Cu}}\mu_{\text{Cu}}]. \quad (1)$$

In this equation, ΔG_{slab} is the Gibbs free energy of a slab model representing the surface, and ΔN_{O} and ΔN_{Zn} are the number of oxygen and zinc atoms, respectively. These quantities are all given relative to a slab of the same size representing the bulklike ZnO(0001) surface. The number of copper atoms in the slab and the in-plane surface area are denoted N_{Cu} and A, respectively. We do not need to account for the terminating quasiatoms in this relative free-energy expression, as their number will cancel between the surface structure under consideration and the bulklike ZnO(0001) reference.

The three chemical potentials μ_{O}, μ_{Zn}, and μ_{Cu} are determined by the environment that the surface is exposed to. Specifically, the surface is assumed to be in thermodynamic equilibrium with the ZnO bulk underneath, which imposes the constraint that the sum of μ_{O} and μ_{Zn} equals the free energy of bulk ZnO; that is,

$$\mu_{\text{O}} + \mu_{\text{Zn}} = G_{\text{ZnO}}. \quad (2)$$

Inserted into Eq. (1), this constraint leads to the following expression of the surface free energy in terms of the copper and oxygen chemical potentials:

$$\Delta\gamma = \frac{1}{A}[\Delta G_{\text{slab}} - \Delta N_{\text{Zn}} G_{\text{ZnO}} - (\Delta N_{\text{O}} - \Delta N_{\text{Zn}})\mu_{\text{O}} - N_{\text{Cu}}\mu_{\text{Cu}}]. \quad (3)$$

Following common practice (e.g., Refs. 34–36,42, and 44), we approximate the Gibbs free energy, G, of all condensed phases (surface and bulk) with the DFT energy, E, neglecting the temperature and pressure/volume dependence in these terms. Accordingly, we replace ΔG_{slab} and G_{ZnO} in Eq. (3) with ΔE_{slab} and E_{ZnO}, respectively.

With these approximations, the only explicit pressure and temperature dependence is retained in the oxygen chemical potential, μ_{O}. The variation of μ_{O} with respect to the oxygen partial pressure and temperature is calculated using an ideal-gas approximation and thermochemical tabulations (see, e.g., Ref. 34 for details). The chemical potential of copper, μ_{Cu}, is used here as a more abstract measure of the exposure of the

surface to copper. Detailed numerical values will depend on the mode of delivery of copper atoms to the surface.

It is convenient to express the chemical potentials as relative values, $\Delta\mu$, to some well-defined references. For μ_{Cu} and μ_{O}, these references are, respectively, the DFT energies of bulk copper, E_{Cu}, and molecular oxygen, $1/2\ E_{\mathrm{O}_2}$; that is,

$$\Delta\mu_{\mathrm{Cu}} = \mu_{\mathrm{Cu}} - E_{\mathrm{Cu}} \quad \text{and} \quad \Delta\mu_{\mathrm{O}} = \mu_{\mathrm{O}} - \tfrac{1}{2}E_{\mathrm{O}_2}. \tag{4}$$

Note here that oxygen is referenced to $1/2\ E_{\mathrm{O}_2}$, which corresponds to the Gibbs free energy at standard pressure and a temperature of 0 K. This needs to be taken into account when comparing our chemical potentials with thermochemistry data which are referenced to standard conditions, namely, $p^\circ = 1$ atm and $T^\circ = 298.15$ K. Specifically, the oxygen chemical potential at standard conditions, $\Delta\mu_{\mathrm{O}}^\circ$, evaluates to $-\frac{1}{2}T^\circ S_{\mathrm{O}_2}^\circ$, or -0.32 eV per oxygen atom, using the experimental value of $S_{\mathrm{O}_2}^\circ = 205.2$ J/mol K (Ref. 54) for the standard entropy of oxygen.

The meaningful and allowable range over which $\Delta\mu_{\mathrm{O}}$ and $\Delta\mu_{\mathrm{Cu}}$ can be varied is subject to limits that are determined by several reactions between the surface, bulk, and gas phases. The upper bounds for $\Delta\mu_{\mathrm{Cu}}$ and $\Delta\mu_{\mathrm{O}}$ are both located at 0 eV. Above these boundaries, large amounts of molecular oxygen and bulk copper will condense in the system. The lower bound for $\Delta\mu_{\mathrm{O}}$ is given by the point at which the bulk ZnO substrate is reduced to zinc metal. This occurs when the reduction reaction is exergonic, that is, when

$$G_{\mathrm{Zn}} + \mu_{\mathrm{O}} - G_{\mathrm{ZnO}} \leqslant 0, \tag{5}$$

which resolves to the following constraint on $\Delta\mu_{\mathrm{O}}$:

$$\Delta\mu_{\mathrm{O}} \leqslant E_{\mathrm{ZnO}} - E_{\mathrm{Zn}} - \tfrac{1}{2}E_{\mathrm{O}_2}, \tag{6}$$

where again we have approximated the Gibbs free energy of the condensed phases with the DFT energy.

Another bound on $\Delta\mu_{\mathrm{O}}$ and $\Delta\mu_{\mathrm{Cu}}$ is imposed by the formation of bulk copper oxides. The two copper oxide phases considered here are cuprous oxide (Cu_2O) and cupric oxide (CuO).[55] Analogous to Eq. (6), formation of Cu_2O and CuO occurs when the following inequalities between the chemical potentials are satisfied:

$$\Delta\mu_{\mathrm{O}} + 2\Delta\mu_{\mathrm{Cu}} \geqslant E_{\mathrm{Cu_2O}} - 2E_{\mathrm{Cu}} - \tfrac{1}{2}E_{\mathrm{O}_2} \tag{7}$$

and

$$\Delta\mu_{\mathrm{O}} + \Delta\mu_{\mathrm{Cu}} \geqslant E_{\mathrm{CuO}} - E_{\mathrm{Cu}} - \tfrac{1}{2}E_{\mathrm{O}_2}. \tag{8}$$

Last, we note that there is no obvious lower bound on $\Delta\mu_{\mathrm{Cu}}$; however, we find that below a certain threshold, Cu-containing surface phases are no longer stable, which for all intents creates a practical lower bound.

C. Chemical potential scaling

The oxygen chemical potential is our primary point of contact with the "real world," allowing us to assess the temperature and oxygen partial pressure conditions under which a given phase may be expected to occur in experiment. It is therefore prudent to assess the accuracy of our calculated chemical potentials by comparison to suitable experimental data. To this end, we consider the formation of bulk metal oxides from their constituent elements according to the generic reaction

$$xM + \tfrac{1}{2}\mathrm{O}_2 \rightleftharpoons M_x\mathrm{O}. \tag{9}$$

The Gibbs free energy of reaction for this process is denoted $\Delta_f G_{M_x\mathrm{O}}$ and is highly dependent on pressure and temperature. We are specifically interested here in those conditions when metal oxide and pure metal coexist, which requires that $\Delta_f G^*_{M_x\mathrm{O}} = 0$. A superscripted asterisk is used here to indicate these critical conditions, which correspond to a certain *transition chemical potential*, $\Delta\mu_{\mathrm{O}}^*$ or, equivalently, a unique pressure p^* for a given temperature T^*. With these definitions, we further write $\Delta_f G^*_{M_x\mathrm{O}}$ in terms of the Gibbs free energy at standard conditions, $\Delta_f G^\circ$, and approximate the free-energy change between (p^*,T^*) and (p°,T°) by the corresponding change in the oxygen potential, that is,

$$\Delta_f G^*_{M_x\mathrm{O}} \approx \Delta_f G^\circ_{M_x\mathrm{O}} - \left[\Delta\mu_{\mathrm{O}}^* - \Delta\mu_{\mathrm{O}}^\circ\right] = 0, \tag{10}$$

which resolves to the critical chemical potential as follows:

$$\Delta\mu_{\mathrm{O}}^* = \Delta_f G^\circ_{M_x\mathrm{O}} - \tfrac{1}{2}T^\circ S^\circ_{\mathrm{O}_2}. \tag{11}$$

In this form, we can calculate the transition chemical potential from experimental data, using tabulated thermochemical quantities for $\Delta_f G^\circ_{M_x\mathrm{O}}$ and $S^\circ_{\mathrm{O}_2}$ (e.g., Ref. 54).

For the corresponding DFT result, we write out in Eq. (11) the definition of $\Delta_f G^\circ_{M_x\mathrm{O}}$ in terms of its reactant and product contributions, G. This gives

$$\Delta\mu_{\mathrm{O}}^* = G^\circ_{M_x\mathrm{O}} - xG^\circ_M - \tfrac{1}{2}G^\circ_{\mathrm{O}_2} - \tfrac{1}{2}T^\circ S^\circ_{\mathrm{O}_2}, \tag{12}$$

wherein we can cancel the entropy term with the one contained in $G^\circ_{\mathrm{O}_2}$. We also substitute, as before, $G^\circ_{M_x\mathrm{O}}$ and G°_M with the calculated DFT energies to obtain

$$\Delta\mu_{\mathrm{O}}^* = E_{M_x\mathrm{O}} - xE_M - \tfrac{1}{2}E_{\mathrm{O}_2}, \tag{13}$$

which serves as our DFT approximation of the transition chemical potential. Note that this expression is related to the constraint Eqs. (6) to (8) for the special case applicable here, namely, $\Delta\mu_{\mathrm{M}} = 0$ eV (i.e., the system in contact with bulk metal).

In Table II we compare the calculated transition chemical potential [Eq. (13)] with experiment [Eq. (11)] for the three oxides of primary interest to this work, namely, ZnO, Cu_2O, and CuO, and two other oxides in the vicinity of the periodic table (Ag_2O and CdO). The transitions of these five oxides neatly cover the oxygen chemical potential range of interest to this work. The data reveal that in all five cases the DFT result is an underestimate by approximately 25%. For example, the transition chemical potential for ZnO is calculated to be -2.90 eV, which is considerably smaller than the experimental value of -3.64 eV. Similarly, for Cu_2O, we obtain -1.31 eV to be compared with -1.83 eV in experiment.

Such rather large errors in the predicted transition potentials are of some concern, as they would translate into considerable *order-of-magnitude* errors in the predicted transition pressures. In order to address this, we introduce a simple scale factor, ξ, as a surprisingly effective correction. Scaled chemical potentials

TABLE II. Calculated transition chemical potentials (in eV per oxygen atom) for several bulk metal/metal oxide equilibria. We report these energies as directly calculated by DFT [Eq. (13)] and after application of the ξ scale factor [Eq. (14)]. Also reported for comparison are the experimental Gibbs free energies of formation, $\Delta_f G^\circ_{M_xO}$, shifted by $-(1/2)S^\circ_{O_2}T^\circ$ to account for the 0 K reference used in the definition of $\Delta\mu_O$. Experimental data taken from Ref. 54.

Oxide	DFT (Direct) $\Delta\mu^*_O$	DFT (Scaled) $\Delta\tilde{\mu}^*_O$	Experimental $\Delta_f G^\circ_{M_xO}$-$\frac{1}{2}S^\circ_{O_2}T^\circ$
ZnO	−2.90	−3.64[a]	−3.64[a]
CdO	−2.11	−2.65	−2.69
Cu_2O	−1.31	−1.64	−1.83
CuO	−1.23	−1.55	−1.66
Ag_2O	−0.34	−0.43	−0.43

[a]Equality between $\Delta\tilde{\mu}_O$ and experimental value by construction [see Eq. (14)].

(indicated by a tilde) are introduced as follows:

$$\Delta\tilde{\mu}_O = \xi\Delta\mu_O \quad \text{and} \quad \Delta\tilde{\mu}_{Cu} = \xi\Delta\mu_{Cu}. \tag{14}$$

The specific value chosen here is $\xi = 1.257$ for which the ZnO transition potential, and thus, the lower bound on the $\Delta\tilde{\mu}_O$ scale, matches the experimental value of −3.64 eV. As Table II confirms, there is now much better agreement for the other four oxides as well. Residual errors in $\Delta\tilde{\mu}_O$ of less than 0.2 eV are much more tolerable for the purpose of this work.

D. Stacking notation

For the following discussions, it is useful to introduce a simple notation to describe the atomic layer structures of the numerous surface reconstructions that we consider. These reconstructions differ principally in the elemental composition and the relative registry of hexagonal atomic planes.

In the hexagonal plane, there are three distinct high-symmetry positions, namely, (0;0), $(\frac{1}{3};\frac{2}{3})$, and $(\frac{2}{3};\frac{1}{3})$ in fractional coordinates that we denote using superscripts A, B, and C, respectively. Using this notation, we can simply describe the layer stacking in bulk wurtzite ZnO along the [0001] axis as $\cdots Zn^AO^BZn^BO^AZn^AO^B\cdots$, where the dots ("$\cdots$") on either end indicate the continuation into bulk. A surface is described by omitting the dots on the surface side. Accordingly, the Zn-terminated Zn(0001) surface is described as $Zn^AO^BZn^BO^A\cdots$, where we introduce the additional convention that the surface-nearest and surface-next-nearest Zn plane define the A and B positions, respectively. When needed, we use numerical subscripts to indicate fractional occupation of an atomic plane in units of monolayer (ML); for example, a 1/4-ML coverage of copper adatoms at the fcc site on the ZnO(0001) surface is denoted as $Cu^C_{1/4}Zn^AO^BZn^BO^A\cdots$ (see structure in Fig. 1). Brackets and appropriate subscripts are used to indicate when two atom types share the same atomic plane; for example, $(Zn^A_{2/3}Cu^A_{1/3})O^BZn^BO^A\cdots$ describes a ZnO(0001) surface alloy phase in which one-third of the surface zinc atoms are replaced by copper atoms.

Two clarifications on our notation should be noted. First, when referring to atoms at A, B, and C positions, we do not imply that these atoms are rigidly fixed at these sites. In the course of geometry optimization, atoms may relax away somewhat from an ideal symmetry position. Our notation is only meant to provide an approximate indication of the in-plane position. Second, the positions of adatoms on the ZnO(0001) surface are also commonly referred to as *fcc*, *hcp*, and *top* sites. These labels are distinguished from our notation in that they denote an in-plane position *relative* to the two nearest atomic layers below. For example, on a $Zn^AO^B\cdots$ surface, the top, hcp, and fcc positions correspond to the A, B, and C sites, respectively. In contrast, on a $Cu^CO^AZn^AO^B\cdots$ surface, C is the top site, A is the hcp site, and B is the fcc site. We switch between these two notations depending on whether a relative or absolute positional reference better serves the discussion.

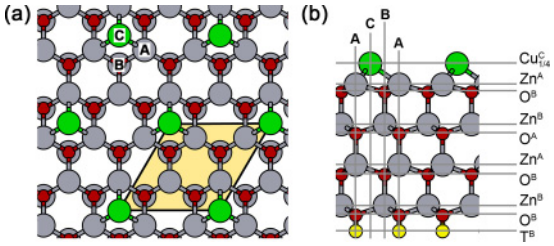

FIG. 1. (Color online) A quarter monolayer (1/4 ML) coverage of copper adatoms on the ZnO(0001) surface at the fcc site which is the C site in our absolute stacking notation. (a) Top view. The copper, zinc, and oxygen atoms are represented by large dark (green) and lighter gray circles, and small dark (red) circles, respectively. The three high-symmetry sites in the hexagonal plane that define the stacking sequence (see text) are labeled with the letters A, B, and C, respectively. The (2 × 2) surface unit cell is indicated using background shading. (b) Side view illustrating the $Cu^C_{1/4}Zn^AO^BZn^BO^A\cdots$ stacking sequence of atomic layers. The slab-terminating quasiatoms (T) are indicated by small (yellow) circles.

E. A note on surface stoichiometry

There is some ambiguity in the literature about how to describe the stoichiometry of an oxide overlayer on the ZnO(0001) surface. Contributing to this ambiguity are two complicating facts, namely, that the [0001] direction is polar in zinc oxide and that the bulklike surface termination itself is nonstoichiometric (oxygen-deficient).

In order to arrive at what we believe is the correct approach to surface stoichiometry, it is convenient to consider a $Zn(O_{1/4})_4$ tetrahedron to be the basic building block of zinc oxide (see also Refs. 44 and 56). This building block is composed of a central Zn cation with a nominal charge of +2 surrounded by four quarters of an oxide anion, with each quarter having a nominal charge of −1/2. This partitioning splits each oxygen anion (full nominal charge of −2) into four parts and attributes these parts to the four Zn cations that the oxygen is bonded to. Importantly, this tetrahedral building block is characterized as stoichiometric, charge neutral, and with a zero dipole. These characteristics also apply to any structure entirely composed of such building blocks.

Along the [0001] direction, the $Zn(O_{1/4})_4$ building block is written in terms of our stacking notation as $[O^A_{1/4}Zn^AO^B_{3/4}]$ (or other permutations of the three sites A, B, C). Considering now the bulklike ZnO(0001) surface (stacking sequence $Zn^AO^BZn^BO^A\cdots$) in terms of these building blocks, one can

see that an incomplete $[Zn^{A}O^{B}_{3/4}]$ building block, lacking the $O^{A}_{1/4}$ plane, is required to construct the surface. It is the absence of these 1/4-ML oxygen atoms that produces the nominal nonstoichiometry and surface dipole of the bulklike ZnO(0001) termination.

In the following discussion, we define the stoichiometry of any copper oxide overlayer relative to a stoichiometric ZnO substrate; that is, we always attribute 1/4-ML oxygen atoms toward creating a stoichiometric ZnO substrate and then determine the overlayer stoichiometry from the atoms that are left over. For example, we discuss in the Results section below a phase characterized by the stacking sequence $Cu^{C}O^{A}Zn^{A}O^{B}\cdots$, that is, a monolayer of copper atoms and a monolayer of oxygen atoms on top of a bulklike ZnO(0001) surface. From the oxygen layer, we attribute 1/4 ML to create a stoichiometric ZnO(0001) surface as discussed above. This leaves 1-ML Cu atoms and 3/4-ML oxygen atoms to form the nominal copper oxide; hence, the stoichiometry of the overlayer is Cu_4O_3. We refer to this structure later on as the Cu_4O_3-ZnO(0001) phase.

We also find it convenient in the following to express the nonstoichiometry of a given surface structure using a quantity that is referred to as an *oxygen excess* Γ_O (see, e.g., Refs. 32 and 57). For the type of slab model used in this work, the oxygen excess is calculated as

$$\Gamma_O = \frac{1}{A}(N_O - N_{Zn}) - \frac{1}{4}\mathrm{ML}, \qquad (15)$$

where N_{Zn} and N_O are the number of zinc and oxygen atoms in the slab and A is the surface area of the slab. The second term accounts for the 1/4-ML oxygen deficiency of the bulklike ZnO(0001) surface (for which $N_{Zn} = N_O$).

III. RESULTS

A. Overview

In our broad survey of possible Cu/ZnO(0001) surface structures we have considered more than 400 configurations that differ in the surface unit cell, elemental composition (Zn, Cu, O), or the relative positioning of atomic planes. This includes structures with copper, oxygen, and copper oxide adsorbed on the ZnO(0001) surface and structures in which copper substitutes for zinc atoms in the surface. We have also extensively surveyed the Cu-free ZnO(0001) surface, in particular, oxygen adatoms and zinc vacancies in the surface and also the so-called triangular pit reconstructions.[44,46,58] The latter group of structures are needed here so that we can describe the transition between the Cu-containing and Cu-free surface regimes.

The relative stability of these surface structures is assessed using the calculated free energies as given by Eq. (3). For given chemical potentials $\Delta\tilde{\mu}_O$ and $\Delta\tilde{\mu}_{Cu}$, the structure with the lowest surface free energy is the one expected to form. The results of our calculations will be discussed in terms of one- and two-dimensional phase stability diagrams, which indicate the most stable (i.e., lowest free energy) structure as a function of $\Delta\tilde{\mu}_O$ and/or $\Delta\tilde{\mu}_{Cu}$. As we report, a vast majority of the considered structures is not stable anywhere within the valid phase boundaries.

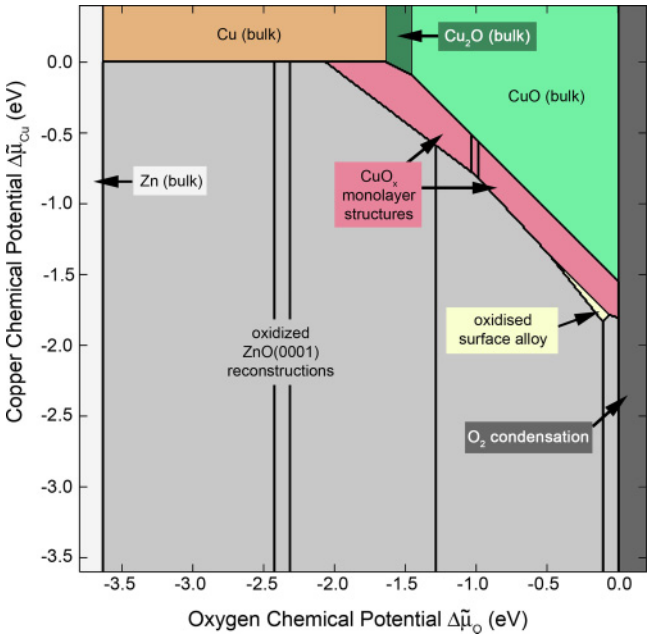

FIG. 2. (Color online) Two-dimensional phase diagram showing the principal surface structures regimes of the Cu/ZnO(0001) system as a function of the scaled copper and oxygen chemical potentials $\Delta\tilde{\mu}_O$ and $\Delta\tilde{\mu}_{Cu}$. Clean ZnO(0001) triangular pits (Refs. 46 and 44) in the center of the diagram and thin CuO_x overlayer reconstructions toward the upper right hand side are framed by bulk precipitates (Zn, Cu, Cu_2O, CuO) and O_2 condensation on three sides.

We start our discussion with an overview of our results in the form of the two-dimensional phase diagram shown in Fig. 2. This diagram delineates eight major regions in $\Delta\mu_O$ and $\Delta\mu_{Cu}$ space in which different types of structures are preferred.

Five of these regions arise from the constraints imposed on $\Delta\tilde{\mu}_O$ and $\Delta\tilde{\mu}_{Cu}$ as discussed above, namely, (1) the ZnO substrate is reduced to metallic zinc at $\Delta\tilde{\mu}_O < -3.64$ eV, (2) molecular oxygen condenses at $\Delta\tilde{\mu}_O > 0$ eV, (3) bulk copper precipitation occurs at $\Delta\tilde{\mu}_{Cu} > 0$ eV, and (4),(5) bulk Cu_2O and CuO precipitation occurs as per Eqs. (7) and (8), respectively. Between these constraints, there exist three regions of stable surface reconstruction. For sufficiently low copper exposure (i.e., a sufficiently negative value of $\Delta\tilde{\mu}_{Cu}$), the surface reconstructions are those of the Cu-free ZnO(0001) surface. These reconstructions have already been described[44,46,48,49] in some detail as a series of triangular pit reconstructions. A second large region is formed at high copper and oxygen chemical potentials. As we show, this region features three types of stable copper oxide monolayer phases on the ZnO(0001) surface. A third, comparatively narrow, region of surface alloys is evident at very high oxygen potentials, where Cu atoms are found to partially substitute for Zn atoms in the oxidized ZnO(0001) surface. This latter region appears as an intermediate between the Cu-oxide overlayer and the Cu-free surface phases. In the following sections, we discuss these surface phase regions in turn, surveying numerous conceivable structures within these regions and identify those that appear as thermodynamically stable in the phase diagram. Our results allow us to shed light on some

of the recent experimental findings of this industrially highly relevant surface science system.

B. Oxygen adsorption and triangular pit reconstructions on the ZnO(0001) surface

We start by considering the ZnO(0001) surface in the absence of any Cu adsorption. This is the prevailing regime at low $\Delta\tilde{\mu}_{\mathrm{Cu}}$ in the lower half of our phase diagram (Fig. 2) and it provides the background against which we later assess the stability of the Cu-containing phases.

Due to the work of Dulub, Kresse, and Diebold,[44,46] with later refinements by Valtiner *et al.*,[48,49] the phases in this regime are now well understood to reconstruct into characteristic *triangular pits*. The partial removal of the surface ZnO double layer renders these structures oxygen rich, which stabilizes the polar ZnO(0001) surface in a slightly more effective way than simple oxygen adatom or zinc vacancy structures.[44] Valtiner *et al.*[48] have recently argued that oxygen adatom structures become favored by thermal free-energy effects under high-temperature conditions. In the light of these findings, it is probably valid to assume that triangular pit and oxygen adatom reconstructions are in coexistence on the ZnO(0001) surface. We repeat herein calculations on these Cu-free ZnO(0001) phases to obtain free energies consistent with our DFT formalism.

Oxygen adatoms. Figure 3 shows for a range of coverages our calculated adsorption energies for oxygen adatoms at three high-symmetry sites. These energies are calculated using the expression

$$E_{\mathrm{ads}} = \frac{1}{n}\left(\Delta E_{\mathrm{slab}} - \frac{n}{2}E_{\mathrm{O_2}}\right), \tag{16}$$

where $E_{\mathrm{O_2}}$ is the energy of molecular oxygen, $\Delta E_{\mathrm{slab}} = E_{\mathrm{O(a)}} - E_{\mathrm{ZnO(0001)}}$ is the energy difference of a relaxed bulklike surface slab with and without oxygen adatoms, respectively, and n is the number of oxygen atoms adsorbed on the slab. Varying oxygen coverages between 1/16 and 1 ML are represented using surface unit cells ranging in size from (1×1) to (4×4). Figure 3 shows that the fcc adsorption site is preferred at all adatom coverages, in agreement with earlier work.[44] The adsorption energy becomes less negative with increasing coverage, consistent with an increased repulsion between the adsorbate atoms. We note in passing that fcc oxygen adatoms become spin polarized at coverages greater than 1/4 ML (i.e., at positive oxygen excess Γ_{O}), while lower coverages do not sustain a stable spin moment. In particular, we find for 1/3- and 1/2-ML $\mathrm{O_{fcc}}$ a total surface magnetic moment of 1/6 and 1/2 μ_{B} per (1×1) unit, respectively, which neatly correlates with the respective Γ_{O} of $+1/12$ and $+1/4$ ML. This shows that the valence-band holes associated with these two oxygen-rich (and thus electron-deficient) structures are fully polarized.

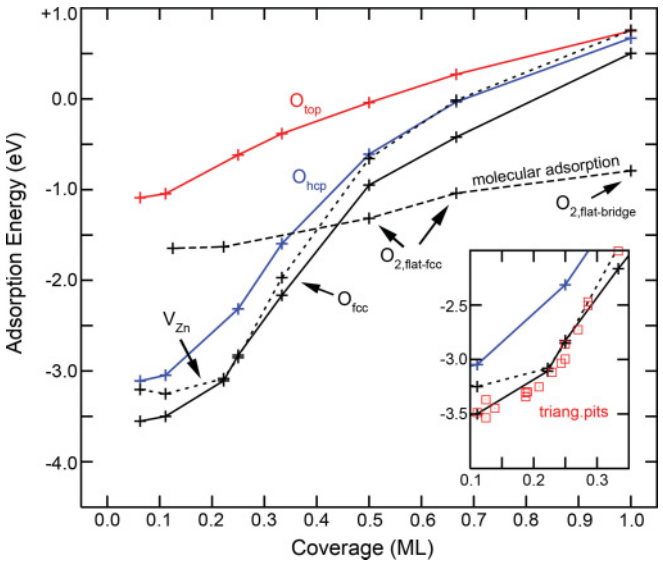

FIG. 3. (Color online) Calculated adsorption energy (in eV per atom) of oxygen adatoms at fcc, hcp, and top sites on the bulklike ZnO(0001) surface as a function of adatom coverage. Also shown is the effective oxygen adsorption energy calculated for zinc vacancies (V_{Zn} [see Eq. (17)] plotted vs vacancy coverage) and molecularly adsorbed oxygen (plotted vs oxygen *atom* coverage). The inset graph highlights the same data for coverages between 0.10 and 0.35 ML, and includes additionally the effective adsorption energies of the triangular pit reconstructions as open (red) square data points.

For all the oxygen adatom configurations considered, we plot in Fig. 4 the calculated surface free energy as a function of the oxygen chemical potential. The resultant minimum free-energy curve (red line) reflects the gradual accumulation of oxygen adatoms on the surface with increasing $\Delta\tilde{\mu}_{\mathrm{O}}$. This starts in the the oxygen-poor limit (−3.6 eV; left-hand side of Fig. 4) with an adatom coverage of 1/9 ML and goes via a 2/9- and 1/4-ML coverage to a maximum coverage of 1/3 ML in the oxygen-rich limit (far right-hand side). Coverages higher than 1/3 ML and lower than 1/9 ML are found to be thermodynamically unstable across the allowable $\Delta\tilde{\mu}_{\mathrm{O}}$ range; this includes the bulklike (i.e., adatom free) ZnO(0001) surface.

Zinc vacancies. Zinc vacancies provide a competing mechanism to render the ZnO(0001) surface oxygen rich. In order to facilitate comparison with oxygen adatoms, we follow Ref. 44 and evaluate for zinc vacancies an effective oxygen adsorption energy using the following expression:

$$E_{\mathrm{ads}} = \frac{1}{n}\left(\Delta E_{\mathrm{slab}} + nE_{\mathrm{ZnO}} - \frac{n}{2}E_{\mathrm{O_2}}\right). \tag{17}$$

In this equation, $\Delta E_{\mathrm{slab}} = E_{\mathrm{Zn(vac)}} - E_{\mathrm{ZnO(0001)}}$ is the energy difference between a bulklike ZnO(0001) surface slab with and without n zinc vacancies. E_{ZnO} is the energy of a formula unit of bulk zinc oxide. The calculated adsorption energies for vacancy coverages between 1/16 and 1 ML are included in Fig. 3 as a dashed line. We see that for most coverages, zinc vacancies are less stable than fcc oxygen adatoms. However, for coverages of 2/9 and 1/4 ML, the energy difference between oxygen adatoms and zinc vacancies becomes very small, entirely consistent with the earlier findings of Kresse *et al.* [see Fig. 7(a) in Ref. 44]. These results suggest that oxygen adatoms and zinc vacancies coexist on ZnO(0001) for a large fraction of the $\Delta\tilde{\mu}_{\mathrm{O}}$ range in Fig. 4.

As for oxygen adatoms, we find that high coverages of zinc vacancies result in spin polarization. A 1/2-ML coverage of vacancies with a $c(2 \times 2)$ repeat, for example, has a calculated surface magnetic moment of 0.50 μ_B per (1×1) unit, which again indicates full polarization of the electron holes in the valence band. In contrast, the 1/3-ML vacancy structure did not sustain a stable magnetic moment, preferring to relax to a spin-paired solution.

Molecular oxygen adsorption. We also explored the possibility of oxygen binding molecularly to the ZnO(0001) surface which could plausibly occur at sufficiently high $\Delta\tilde{\mu}_O$, that is, just prior to the $\Delta\tilde{\mu}_O = 0$ eV condensation point. Using $(\sqrt{3} \times \sqrt{3})$, (2×2), and (3×3) unit cells for nominal oxygen atom coverages, θ_O, of 2/9, 1/2, and 2/3 ML, respectively, we tested six bonding configurations of an O_2 admolecule on ZnO(0001), namely a *vertically* oriented molecule at top, fcc, and hcp sites, as well as a horizontally flat molecule at fcc, hcp, and bridge sites. Table III reports our calculated adsorption energies for these configurations.

Favored at 2/9-, 1/2-, and 2/3-ML coverage is the flat-fcc configuration. In this configuration the molecule is positioned above three Zn atoms at an fcc site, binding with one oxygen atom to two zinc atoms and with the other oxygen atom to a third zinc atom. The corresponding flat-hcp configuration is approximately 0.1 eV less stable per oxygen atom, and the three vertically oriented configurations are less stable by more than 0.5 eV. At higher coverages the flat-bridge configuration becomes important in which the oxygen molecule bridges between two surface zinc atoms in a near-planar, trapezoidal Zn–O–O–Zn configuration. Unstable at 2/9 and 1/2 ML, the flat-bridge is the second most stable configuration at 2/3 ML and becomes the preferred configuration at 1 ML in a $c(2 \times 2)$ unit cell. We note that the flat-fcc configuration was found to be unstable at 1-ML coverage, spontaneously relaxing to a flat-bridge configuration.

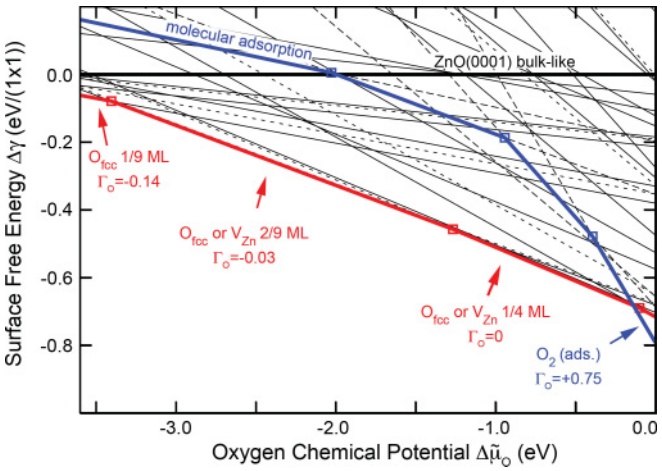

FIG. 4. (Color online) Phase stability diagram with respect to the oxygen chemical potential, $\Delta\mu_O$, for oxygen adatoms (O_{fcc}, O_{hcp}, and O_{top}; solid lines), zinc vacancies (V_{Zn}; dotted lines) and flat-fcc molecular oxygen adsorbates (dashed lines) on bulklike ZnO(0001). The combined minimum free-energy curve of oxygen adatoms and zinc vacancies is plotted as a thick (red) line. The minimum free-energy curve of the molecular oxygen adsorbate structures is plotted as a thick (blue) line. The oxygen excess, Γ_O, of selected phases is indicated in units of ML.

TABLE III. Calculated adsorption energies of oxygen molecules in six binding orientations and four coverages on the ZnO(0001) surface. Also given for comparison is the adsorption energy for a molecule dissociated into two O_{fcc} adatoms. Configurations that are not stable (n.s.) during optimization are indicated as such. All energies are reported in eV per oxygen atom. Note that the oxygen coverage, θ_O, refers to the number of oxygen *atoms* per unit area. The oxygen molecule coverage is smaller by a factor of two.

Coverage θ_O	(3×3) 2/9 ML	(2×2) 1/2 ML	$(\sqrt{3} \times \sqrt{3})$ 2/3 ML	$c(2 \times 2)$ 1 ML
Flat-fcc	−1.63	−1.31	−1.04	n.s.
Flat-bridge	n.s.	n.s.	−0.99	−0.79
Flat-hcp	−1.53	−1.19	−0.93	—
Vertical-fcc	−0.82	−0.67	−0.56	—
Vertical-hcp	−0.70	−0.51	−0.43	—
Vertical-top	−0.24	−0.30	−0.28	—
Dissociated	−3.11	−0.95	−0.42	+0.50

Of particular interest in these data is the stability of molecularly adsorbed oxygen relative to an equivalent coverage of oxygen adatoms. The adsorption energy of this dissociated configuration is included in Table III for comparison. The data reveal that at low coverage ($\theta_O = 2/9$ ML) oxygen dissociation is exothermic and the dissociated O_{fcc} adatom configuration is preferred. However, at higher coverages ($\theta_O = 1/2$ ML and above), the nondissociated molecular configurations are preferred. The calculated adsorption energies for the preferred molecular configuration are included in Fig. 3 (see dashed line), illustrating the crossover in preference at a coverage of approximately 0.45 ML. This crossover is also evident in the phase stability diagram (Fig. 4), where the minimum free-energy curve of the flat-fcc/flat-bridge adsorbates is plotted as a thick (blue) line. Above $\Delta\tilde{\mu}_O = -0.14$ eV, a molecular oxygen adsorbate structure [the $\theta_O = 1$ ML flat-bridge $c(2 \times 2)$ phase] becomes favored over the dissociated adatom structures.

The preference for molecular or dissociated adsorption is conveniently examined in terms of molecular dissociation energies, $\Delta E_{dissoc.}$, which are calculated here as twice the per-atom adsorption energy difference between the preferred molecular and adatom configuration. It is instructive to correlate the coverage dependence of $\Delta E_{dissoc.}$ with the surface oxygen excess, Γ_O, and the surface spin moment, μ. Table IV reveals that molecular adsorption is favorable (i.e., $\Delta E_{dissoc.}$ is negative) at positive oxygen excess, that is, for a surface that is electron deficient. In fact, for positive oxygen excess, the correlation between Γ_O and $\Delta E_{dissoc.}$ is very nearly linear. Positive oxygen excess also correlates with the calculated surface spin magnetic moments. As noted above, the moment per unit area, $\mu_{O_{fcc}}/A$, of the dissociated fcc-adatom configurations is twice the oxygen excess, indicating that all valence electron holes (two per excess oxygen adatom) are fully polarized. Comparing now in Table IV the magnetic moments for molecular and dissociated configurations (μ_{O_2} and $\mu_{O_{fcc}}$, respectively), we can see that the molecular moment is smaller by 1.00 μ_B per adsorbed oxygen atom. Taken together, this suggests that the preference for molecular configurations at

TABLE IV. Dissociation energy, $\Delta E_{\text{dissoc.}}$, spin magnetic moment, μ_{O_2}, and oxygen-oxygen bond distance, d_{O-O}, of molecular oxygen adsorbed on ZnO(0001) as a function of oxygen atom coverage, θ_O. Also reported for reference are the oxygen excess Γ_O and the spin magnetic moment, $\mu_{O_{fcc}}$, and moment surface density, $\mu_{O_{fcc}}/A$, of the corresponding dissociated, fcc-adatom configuration.

Coverage θ_O	(3×3) 2/9 ML	(2×2) 1/2 ML	$(\sqrt{3}\times\sqrt{3})$ 2/3 ML	$c(2\times2)$ 1 ML
Γ_O (ML)	−0.03	+0.25	+0.42	+0.75
$\Delta E_{\text{dissoc.}}$ (eV)	+2.96	−0.72	−1.24	−2.58
$\mu_{O_{fcc}}/A$ ($\mu_B/A_{(1\times1)}$)	0	0.50	0.83	1.50
$\mu_{O_{fcc}}$ (μ_B per O atom)	0	1.00	1.25	1.50
μ_{O_2} (μ_B per O atom)	0	0	0.25	0.50
d_{O-O} (Å)	1.514	1.499	1.435	1.347

positive oxygen excess is driven by the pairing of polarized valence electron holes into covalent O–O bonds. For example, in the (2×2) 1/2 ML dissociated case in Table IV, we may simplistically attribute the single hole per oxygen atom[59] to a nominal O^-_{fcc} adsorbate, which would, in atomic terms, have an open-shell s^2p^5 valence configuration, consistent with a spin-moment of 1 μ_B. A covalent bond between two such adatoms gives rise to a O_2^{2-} peroxide species, which has a closed-shell, $\sigma_s^2\sigma_s^{*2}\sigma_p^2\pi_p^4\pi_p^{*4}$ configuration (in diatomic terms) and therefore a zero spin magnetic moment. The argument neatly extends to higher coverages, and we can thus identify the molecular adsorbate in the $c(2\times2)$ 1-ML case as an O_2^- superoxide species with a $\sigma_s^2\sigma_s^{*2}\sigma_p^2\pi_p^4\pi_p^{*3}$ configuration and a magnetic moment of 1/2 μ_B per atom.

Triangular pit reconstructions. In experiment, the triangular pit reconstructions are observed to be highly disordered,[46] superposing a large variety of different triangle sizes and depths (i.e., triangles within triangles) into a large-scale surface structure. Given the length scales involved, our calculations can only cover a limited and artificially ordered subset-representation of these phases. The triangle reconstructions included in our survey are enumerated and labeled in Table V, each characterized by the unit cell used, the size indices n of any triangular depressions within the cell,[60] the number of additional fcc oxygen adatoms and Zn vacancies in the unit cell, and the overall oxygen excess Γ_O. While the set is limited, we believe it to be sufficient to fulfill its primary purpose for this work, which is to establish the $\Delta\tilde{\mu}_O$-dependent free energy of the oxidized ZnO(0001) surface.

Also reported in Table V is an effective average oxygen adsorption energy, E_{ads}, which is obtained by recasting the slab energy into an adsorption energy for those oxygen atoms that are in stoichiometric excess. In a generalization of Eqs. (17) and (16), this energy is calculated as

$$E_{ads} = \frac{\Delta E_{slab} + \Delta N_{Zn} E_{ZnO} - \frac{1}{2}(\Delta N_O - \Delta N_{Zn}) E_{O_2}}{\Delta N_O - \Delta N_{Zn}}, \quad (18)$$

where $\Delta E_{slab} = E_{tp} - E_{ZnO(0001)}$ is the energy difference between two slabs representing a triangular pit and the flat, bulklike ZnO(0001) surface. The difference in the number of zinc and oxygen atoms in the slabs is denoted ΔN_{Zn} and ΔN_O, respectively. As before, E_{ZnO} and E_{O_2} are the energies of bulk ZnO and molecular oxygen. These effective adsorption

TABLE V. Characteristic parameters defining the triangular pit reconstructions considered in this work. Given are the unit cell of the reconstruction, the label used to refer to a structure, the indices n defining the size of a triangular pit,[60] the area of the unit cell A (given in multiples of $A_{(1\times1)}$), the oxygen excess Γ_O (in ML), and the effective oxygen adsorption energy E_{ads} [in eV; see Eq. (18)].

Unit cell	Label	Structure		A	Γ_O	E_{ads}
$(\sqrt{7}\times\sqrt{7})$	T-2	$n=2$		7	+0.04	−2.47
	T-2 + O_{fcc}	$n=2$	+1 O_{fcc}	7	+0.18	−1.26
	T-2 + V_{Zn}	$n=2$	+1 V_{Zn}	7	+0.18	−1.19
$(\sqrt{12}\times\sqrt{12})$	T-3	$n=3$		12	±0.00	−2.86
	T-3 + O_{fcc}	$n=3$	+1 O_{fcc}	12	+0.03	−2.01
(4×4)	T-2	$n=2$		16	−0.12	−3.37
	T-3	$n=3$		16	−0.06	−3.34
$(\sqrt{19}\times\sqrt{19})$	T-4	$n=4$		21	−0.06	−3.30
	T-4-2	$n=4,2$		21	+0.04	−2.50
	T-4-2 + V_{Zn}	$n=4,2$	+1 V_{Zn}	21	+0.08	−1.90
(6×6)	T-4	$n=4$		36	−0.14	−3.49
	T-5	$n=5$		36	−0.11	−3.45
$(\sqrt{37}\times\sqrt{37})$	T-6-3	$n=6,3$		37	−0.01	−3.03
	T-6-3 + O_{fcc}	$n=6,3$	+1 O_{fcc}	37	+0.02	−2.73
$(\sqrt{48}\times\sqrt{48})$	T-6	$n=6$		48	−0.13	−3.53
	T-6 + 3O_{fcc}	$n=6$	+3 O_{fcc}	48	−0.06	−3.31
	T-6-3	$n=6,3$		48	−0.06	−3.30
	T-7-3	$n=7,3$		48	−0.04	−3.25
	T-7-3 + O_{fcc}	$n=7,3$	+1 O_{fcc}	48	−0.02	−3.12
	T-7-3 + 2O_{fcc}	$n=7,3$	+2 O_{fcc}	48	±0.00	−3.00

energies are included in Fig. 3 as an inset with an effective coverage defined as $\theta_O = (\Delta N_O - \Delta N_{Zn})/A$. The adsorption energies of the triangular pits are seen to be closely scattered around the data points of the simple oxygen adatom and zinc vacancies, with some of them more stable. We note as an aside that almost all of the triangular pit structures with positive oxygen excess manifest some form of stable spin polarization in our calculations, whereas those structures with negative and zero Γ_O relax to spin-paired solutions without exception.

The resulting phase stability diagram for these reconstructions is shown in Fig. 5, with the minimum free-energy curve shown in thick blue. The diagram is overlayed for reference with the minimum free-energy curve of the adatom/zinc vacancy/admolecule structures of the bulklike surface (thick red line; taken from Fig. 4). We see that the triangular reconstructions are very slightly preferred over the bulklike surface structures, broadly consistent with earlier calculations.[44,46,48] At very high $\Delta\tilde{\mu}_O$, however, we find a molecular adsorbate structure to take over.

In detail, starting at the oxygen-poor end of the phase diagram (left-hand side of Fig. 5), the first stable surface phase is the (4 × 4) T-3 structure, featuring a single $n=3$ triangular depression and an oxygen excess of $\Gamma_O = -0.06$. The next stable phase at $\Delta\tilde{\mu}_O = -2.43$ eV is the $(\sqrt{48}\times\sqrt{48})$ T-7-3 structure characterized by a $n=3$ triangular pit within a larger $n=7$ pit. This structure has a slightly less negative oxygen excess of $\Gamma_O = -0.04$. At a slightly increased $\Delta\tilde{\mu}_O = -2.32$ eV, a $(\sqrt{37}\times\sqrt{37})$ T-6-3 double triangle becomes preferred, combining a $n=6$ and a $n=3$ triangular pit in a

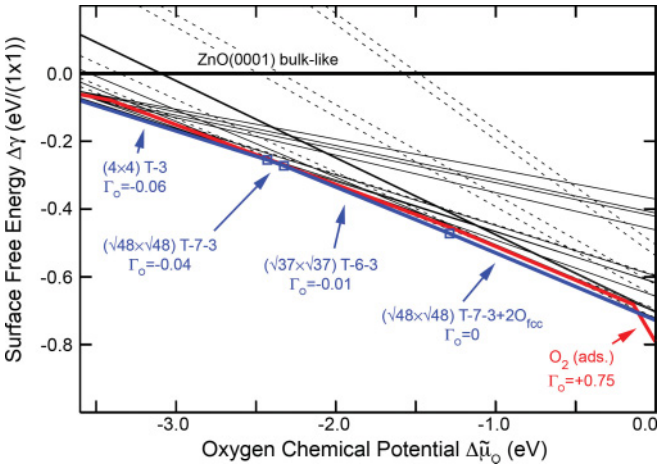

FIG. 5. (Color online) Phase stability diagram of triangular pit reconstructions of the ZnO(0001) surface. Black solid free-energy lines correspond to pure triangular pit reconstructions, while dashed lines represent mixed reconstructions combining triangular pits with oxygen adatoms or zinc vacancies. The resultant minimum free-energy curve for these reconstructions is shown as a thick (blue) solid line. Also included for reference as a thick (red) solid line is the combined minimum free curve of the pure oxygen adatom, zinc vacancy, and molecular oxygen phases (see Fig. 4). The oxygen excess, Γ_O, of selected phases is indicated in units of ML.

slightly smaller unit cell for an oxygen excess of $\Gamma_O = -0.01$. At $\Delta\tilde{\mu}_O = -1.29$ eV, the next transition results in a variant of the $(\sqrt{48} \times \sqrt{48})$ T-7-3 containing two O_{fcc} adatoms (structure shown in Fig. 6). This phase is stoichiometric; that is, the oxygen excess, Γ_O, is zero. This phase is, in turn, taken over at $\Delta\tilde{\mu}_O = -0.11$ eV by the $c(2 \times 2)$ $\theta_O = 1$ ML flat-bridge molecular adsorbate phase.

We note that our phase diagram differs in detail to the earlier results of Kresse *et al.*,[44] Dulub *et al.*,[46] and Valtiner *et al.*[48] in regard to which triangular reconstructions is actually preferred at a given oxygen chemical potential. These differences can be attributed to primarily two factors. First, unlike these earlier works, we scale our chemical potential as discussed in Sec. II C in order to achieve a better match with experimental bulk oxide formation energies. Second, and as already pointed out by Valtiner *et al.*,[48] thermal effects, and their representation in the model, matter in distinguishing which of a large number of closely competing reconstructions is preferred. Additionally, we find that phases containing molecularly adsorbed oxygen have a small window of stability at very high oxygen chemical potentials. Such phases were not considered in these earlier works. For the purpose of the present work, however, we believe these differences in detail are minor ones. All we require for the following discussion is a sufficiently accurate representation of the free energy of the Cu-free ZnO(0001) surface to serve as a reference for the CuO_x overlayer phases.

C. Copper adsorption on bulklike ZnO(0001)

Single copper adatoms. We now investigate structures involving adsorption of copper atoms on the clean ZnO(0001) surface. Copper adatom coverages between 1/16 and 1 ML are considered using a number of surface unit cells including

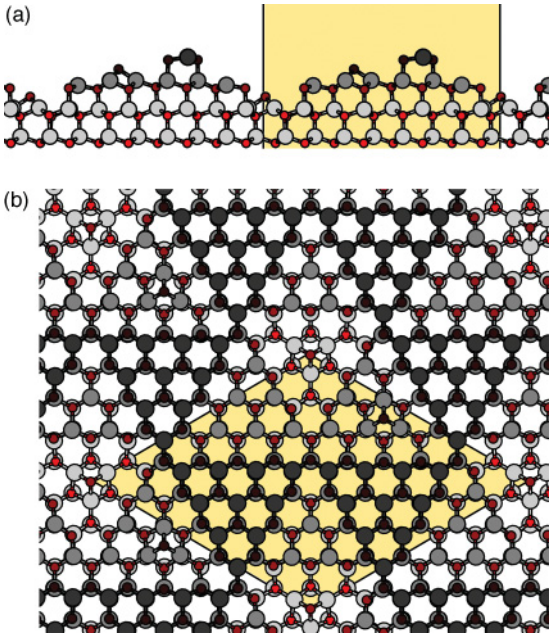

FIG. 6. (Color online) Side and top view of the $(\sqrt{48} \times \sqrt{48})$ T-7-3 + $2O_{fcc}$ structure, one of several phases used in this work to represent the triangular pit reconstruction on the ZnO(0001) surface. The structure shown features a $n = 3$ triangle within a larger $n = 7$ triangle. Two fcc oxygen adatoms are placed on the lower and middle platforms.

(1×1), $(\sqrt{3} \times \sqrt{3})$, (2×2), (3×3), and (4×4). Copper adsorption energies are calculated using the expression

$$E_{ads} = \frac{1}{n}(\Delta E_{slab} - n E_{Cu(atom)}). \quad (19)$$

$E_{Cu(atom)}$ is the energy of a copper atom and $\Delta E_{slab} = E_{Cu(ads)} - E_{ZnO(0001)}$ is the energy difference between a slab of bulklike ZnO(0001) and a slab containing n copper adatoms on the surface. An overview of the coverage-dependent adsorption energies at the three high-symmetry sites fcc, hcp, and top is given in Fig. 7.

In agreement with earlier work,[29,47] we find that the fcc site is the preferred binding site for Cu adatoms, followed by the hcp and the top site. For the lowest coverage considered (1/16 ML), the fcc site has an adsorption energy of −2.81 eV and is slightly (0.05 eV) more stable than than the hcp site and significantly (0.48 eV) more stable than the top site. For higher coverages, the adsorption energies first increase (i.e., adsorption becomes less stable) up to about 1/3 ML and then gradually decrease up to a full monolayer. This indicates a repulsive interaction between Cu adatoms at intermediate separations that is presumably caused by surface strain. At higher coverage, an attractive interaction takes over when Cu atoms occupy adjacent sites.

Detailed numerical comparisons with the earlier work of Meyer *et al.*[28] and Dai *et al.*[29] are made in Table VI. We observe that our adsorption energies for 1/4-ML Cu in a (2×2) unit cell are up to 0.66 eV larger than those reported by Meyer *et al.*[47] for the same coverage. The origin of this discrepancy remains unclear, but does not appear to be associated with slab thickness.[61] We are in much better agreement with the

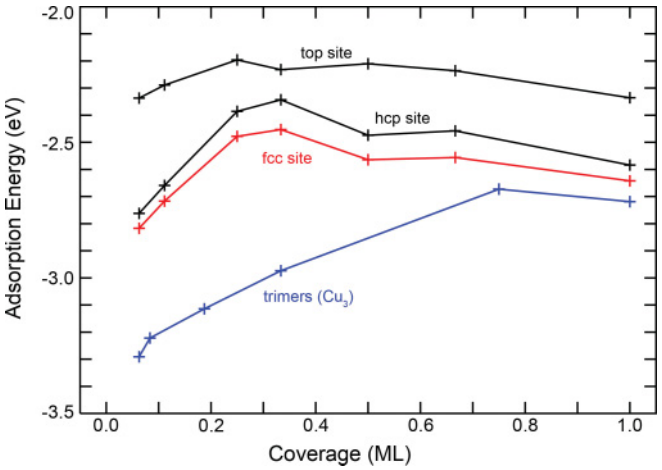

FIG. 7. (Color online) The adsorption energy of Cu atoms (in eV per atom) on the clean ZnO(0001) surface as a function of coverage. Shown are the adsorption energies for single atoms at the high-symmetry fcc, hcp, and top sites, as well the highly stable Cu_3 clusters.

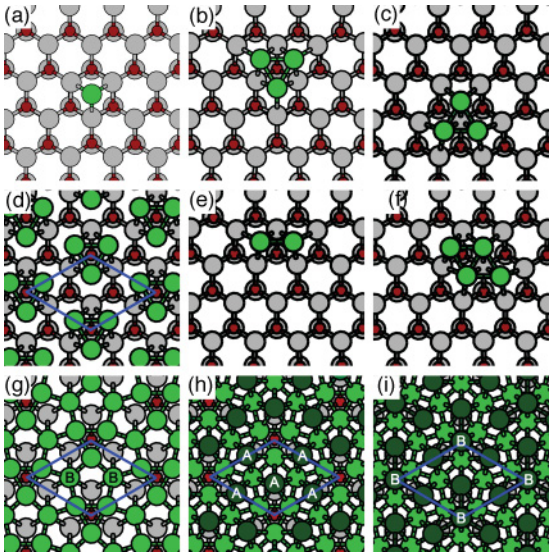

FIG. 8. (Color online) Top view of copper clusters (Cu_n) and cluster-based overlayers on the ZnO(0001) surface. (a) A single copper adatom at an fcc site. (b) A Cu_3 cluster of three adjacent fcc copper adatoms centered over an hcp site. (c) A Cu_3 cluster centered over a top site. (d) A dense packing of hcp-centered Cu_3 clusters into a structure with a $(\sqrt{3} \times \sqrt{3})R30^\circ$ repeat. The Cu coverage in this structure is 1 ML. (e),(f) A dimer, Cu_2, and a tetramer, Cu_4, of fcc-Cu adatoms. (g),(h),(i) Cu overlayer phases with coverages of 5/3, 8/3, and 3 ML based on the Cu_3 structure in panel (d). The positioning of Cu atoms at A and B lattice sites is indicated. Copper, zinc, and oxygen atoms are represented by large dark (green) and lighter gray circles and small dark (red) circles, respectively.

adsorption energies reported by Dai *et al.*[29] for a full monolayer coverage with differences of about 0.1 eV.

Copper adatom clusters. In addition to single Cu atoms at the high-symmetry sites, we have also considered structures where adatoms are clustered into various Cu_n configurations. This generally leads to a significant gain in the adsorption energy. Three Cu atoms at mutually nearest fcc sites in a (3×3) unit cell relax toward each other, forming an equilateral triangle with a Cu–Cu bond distance of 2.52 Å. There are two variants of this fcc-Cu trimer: A trimer centered over an hcp site [Fig. 8(b)] has an adsorption energy of −2.98 eV per Cu atom; a trimer centered over a top site [Fig. 8(c)] is less stable with an adsorption energy of −2.90 eV. We note in passing that four more Cu_3 variants (for a total of six) arise as permutations of Cu site and trimer center over fcc, hcp, and top sites; all are less stable than the hcp-centered trimer of three fcc-Cu atoms [Fig. 8(b)]. Included in Fig. 7 are the coverage-dependent adsorption energies of Cu_3 clusters up to a full monolayer, that is, a dense packing of Cu_3 trimers in a $(\sqrt{3} \times \sqrt{3})R30^\circ$ unit cell [Fig. 8(d)]. At all coverages, we find that Cu_3 clusters are significantly more stable than isolated Cu adatoms.

Copper dimers [Cu_2; Fig. 8(e)] and tetramers [Cu_4; Fig. 8(f)] in a (3×3) unit cell are slightly (≈0.1 eV per atom) less stable than Cu_3 with adsorption energies of −2.86 and −2.87 eV, respectively. In these structures, the Cu atoms are again slightly displaced away from the ideal fcc position toward the other Cu atoms in the cluster. The energetics suggests that there is a competition between two forces in the formation of Cu_n clusters: On the one hand, energy is gained by the pairing of Cu atoms; on the other hand, the shorter Cu–Cu bond lengths relative to the ZnO(0001) surface repeat ($a = 3.289$ Å) exacts a strain penalty as Cu atoms are displaced away from the favored fcc position.

TABLE VI. Calculated adsorption energy (in eV) of copper adatoms on the ZnO(0001) surface as a function of coverage.

	This work				Ref. 29	Ref. 28
	(4×4) 1/16 ML	(3×3) 1/9 ML	(2×2) 1/4 ML	(1×1) 1 ML	(1×1) 1 ML	(2×2) 1/4 ML
fcc	−2.82	−2.72	−2.48	−2.64	−2.54	−2.05
hcp	−2.76	−2.66	−2.39	−2.58	−2.50	−1.86
top	−2.34	−2.29	−2.20	−2.34	−2.39	−1.72

Copper overlayers. We also considered in our exploration of Cu adatom geometries various structures with more than 1 ML of Cu atoms on the ZnO(0001) surface. In the first instance, we examined 2- and 3-ML structures in a (1×1) unit cell, similar to earlier studies by Meyer *et al.*[28] Our 2-ML overlayer structures were generated by permuting two Cu monolayers over the A, B, and C sites. Of the possible six combinations, the stacking sequence $Cu^ACu^CZn^AO^B \cdots$ was preferred with an average per-atom adsorption energy of −2.85 eV. Thus, the first monolayer prefers the fcc site (as in the 1-ML case; see Table VI) and the second monolayer adopts a hcp stacking relative to the Cu and Zn layers below. Note, however, that at least three other stackings, namely, fcc-fcc, hcp-hcp, and hcp-fcc in terms of first monolayer-second monolayer stacking, are energetically within 0.01 eV/(1×1) of the favored fcc-hcp structure. On the favored 2-ML structure we placed a third Cu monolayer at either the B or the C site to create two 3-ML structures. Of these two, the hcp-stacked structure (i.e., $Cu^CCu^ACu^CZn^AO^B \cdots$) is marginally preferable with an average adsorption energy of −2.93 eV per Cu atom; the adsorption energy of the alternate fcc-stacked structure is only

0.01 eV less stable. These (1 × 1) overlayer results are all broadly in agreement with the earlier calculations of Ref. 28.

The stability of the Cu_3 clusters relative to the nonclustered adatom structures, suggests that a dense packing of Cu_3 triangles could provide a more favorable interface between the bulklike ZnO(0001) surface and multiple Cu overlayers. We explored such structures by adding Cu atoms to the 1-ML $(\sqrt{3} \times \sqrt{3})$R30° Cu_3 structure discussed above [Fig. 8(d)]. Two additional Cu atoms per $(\sqrt{3} \times \sqrt{3})$R30° cell placed at the B site produces the 5/3-ML structure shown in Fig. 8(g) with a Cu adsorption energy of −2.94 eV per atom. The addition of three more Cu atoms at the A site leads to the 8/3-ML structure in Fig. 8(h) and a more favorable adsorption energy of −3.08 eV. One more Cu atom at a B site produces the 3-ML structure in Fig. 8(i) and a further stabilization of the adsorption energy to −3.12 eV. As in the case of the (1 × 1) overlayer structures, the Cu_3-cluster-based overlayer structures become more stable as copper atoms are added. More importantly, the cluster-based overlayer structures lead to more stable adsorption energies at coverages between 1 and 3 ML, presumably due to the fractional site occupations and in-plane relaxations possible in a larger $(\sqrt{3} \times \sqrt{3})$R30° unit cell.

Experimental evidence[14,15,21] suggests that copper deposited on ZnO(0001) grows as (111) atomic planes. Calculated adsorption energies for various Cu(111) overlayers are summarized in Table VII. The (1 × 1) lattice mismatch between Cu(111) and ZnO(0001) is −22%, using the calculated bulk repeats of 2.579 and 3.289 Å, respectively. This mismatch is chiefly responsible for why the (1 × 1) Cu overlayer structures discussed above were so much less stable than bulk Cu. A more commensurate lattice match can be achieved by combining suitably chosen supercells of ZnO(0001) and Cu(111). Very effective is the combination of a (4 × 4) Cu(111) overlayer with a (3 × 3) ZnO(0001) surface unit cell, which reduces the mismatch to +5%. For a single Cu(111) atomic plane, that is, 16 Cu atoms placed above 9 surface Zn atoms in a (3 × 3) ZnO(0001) slab, we calculate an average adsorption energy of −3.31 eV per atom; this represents the most stable Cu adsorption energy in our discussion thus far and is quite close to the calculated bulk binding energy of −3.49 eV. The addition of further Cu(111) atomic layers progressively improves the adsorption energy, reaching a value of −3.40 eV at the thickest copper slab considered (five layers).

An even better lattice fit, albeit at higher computational cost, is achieved by matching a (5 × 5) Cu(111) overlayer with a (4 × 4) ZnO(0001) supercell giving a nominal lattice mismatch of −2%. For a single monolayer, the adsorption energy evaluates to −3.26 eV. This arrangement is slightly (0.07 eV per atom) *less* stable than a Cu(111) monolayer and a (4 × 4):(3 × 3) lattice match. The apparent contradiction—lesser stability despite a more favorable mismatch—occurs because a single monolayer of Cu(111) prefers a lattice repeat that is smaller than bulk. As the data in Table VII confirm, only in the case of multiple monolayers of Cu(111) does the overlayer become sufficiently bulklike for the (5 × 5):(4 × 4) combination to be preferred, reaching an average adsorption energy of −3.41 eV for five atomic layers of Cu(111).

Phase stability. The relative stability of the preferred Cu adatom, cluster, and overlayer phases is assessed using the phase stability diagram shown in Fig. 9. This plot includes the free energies of the fcc adatoms shown as dotted black lines and those of the Cu_3 clusters and overlayer phases as solid and dashed lines, respectively. The resultant minimum free-energy curve of these Cu phases is shown in solid thick (red) lines, which is to be compared with the free-energy lines of the bulklike ZnO(0001) surface (horizontal black line) and bulk Cu precipitation (vertical black line). These data make it strikingly clear that *none* of the considered Cu-containing surface phases is thermodynamically stable. For all allowable Cu chemical potentials ($\Delta\tilde{\mu}_{Cu} < 0$ eV), the bulklike ZnO(0001) surface remains the energetically preferred structure. The first crossing of any Cu phase (namely, the five-layer Cu(111) (5 × 5):(4 × 4) structure; see Table VII) with the bulklike Zn(0001) surface occurs at $\Delta\tilde{\mu}_{Cu} = +0.09$ eV. Because this transition takes place at a positive copper chemical potential, it is not expected to occur because it is thermodynamically preferable for Cu atoms to precipitate as bulk Cu (at $\Delta\tilde{\mu}_{Cu} = 0$ eV and above). This result makes sense, considering that in all cases the calculated adsorption energy is less stable than the bulk Cu cohesive energy of −3.49 eV, and this is reflected in our two-dimensional surface phase diagram (Fig. 2) in that no stable Cu adatom/adcluster/overlayer structures appear.

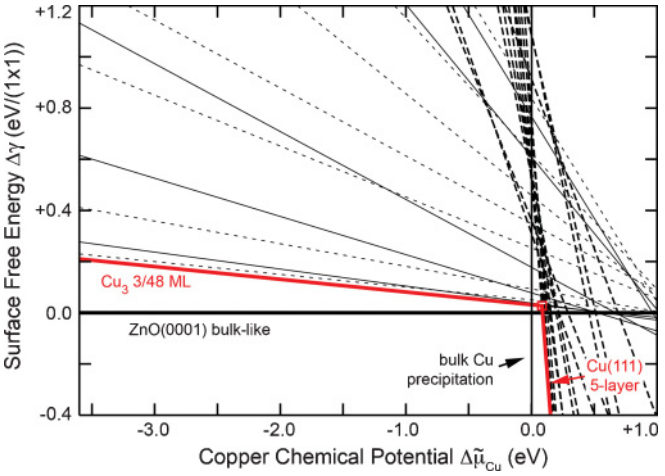

FIG. 9. (Color online) Surface free energy of copper adatoms and copper clusters on the clean ZnO(0001) surface as a function of the copper chemical potential, $\Delta\tilde{\mu}_{Cu}$. Shown are fcc-adatoms (thin dotted lines), Cu_3 clusters (thin solid lines), and the >1-ML overlayer structures (thin dashed lines). The resultant free-energy curve of these Cu phases is shown using thick (red) lines, transitioning from a Cu_3 cluster in a $(\sqrt{48} \times \sqrt{48})$ unit cell (i.e., the Cu coverage is 3/48 ML) directly into a five-layer Cu(111) slab.

D. Copper adsorption on oxidized ZnO(0001)

In this section, we examine how oxidation of the bulklike ZnO(0001) surface affects the energetics of Cu adsorption. In this, we focus primarily on low levels of surface oxidation, namely, oxygen adatom/zinc vacancy coverages of less than 1/4 ML, or, equivalently, a negative oxygen excess Γ_O. Due to the structural variety of the oxidized ZnO(0001) surface (i.e., triangular pits, oxygen adatoms, Zn vacancies; see Sec. III B), we must approach this topic in a more anecdotal fashion, using

TABLE VII. Calculated copper adsorption energies (in eV per atom, relative to free Cu atoms) for various monolayer (ML) coverages and superlattice matchings of a Cu(111) overlayer on a ZnO(0001) substrate. The superlattice mismatch, μ, is also reported based on the calculated lattice constants of 2.579 and 3.289 Å for bulk Cu(111) and ZnO(0001), respectively.

Cu(111)	:	ZnO(0001)	μ (%)	1 ML (eV)	2 ML (eV)	3 ML (eV)	4 ML (eV)	5 ML (eV)
(1×1)	:	(1×1)	−22	−2.65	−2.85	−2.92	—	—
(5×5)	:	(4×4)	−2	−3.26	−3.31	−3.37	−3.40	−3.41
(4×4)	:	(3×3)	+5	−3.31	−3.33	−3.36	−3.38	−3.40
(7×7)	:	(5×5)	+10	−3.22	—	—	—	—

suitable test cases to assess the overall effect. As we show, our test cases point to a common conclusion: Copper adsorption is generally less stable on weakly oxidized ZnO(0001); however, copper and oxygen adatoms attract one another, which leads to a dramatic change in behavior at higher oxidation levels.

Our first test case is the adsorption of a single Cu_{fcc} adatom on a (3×3) bulklike ZnO(0001) surface covered with zero, one, and two oxygen adatoms, corresponding to an oxygen coverage of 0, 1/9, and 2/9 ML, respectively. On the bulklike, nonoxidized surface, the Cu adsorption energy evaluates to −2.72 eV. When 1/9- and 2/9-ML oxygen adatoms are added, the Cu adsorption energy becomes less stable, namely, −2.29 and −1.36 eV, respectively. These energies assume that Cu and O adatoms are positioned at fcc sites furthest from one another in a (3×3) unit cell.

These Cu adsorption energies improve somewhat, when Cu and O adatoms are brought into closer proximity. We find that the preferred configuration for one Cu and one oxygen adatom in a (3×3) unit cell is a Cu-O dimer in which the Cu and O atom are positioned near adjacent hcp and fcc sites, respectively [see Fig. 10(a)]. The Cu adsorption energy for this dimer evaluates to a more favorable −2.41 eV. The reverse configuration—Cu at fcc and O at hcp—is 0.13 eV less stable. Two oxygen adatoms and one Cu adatom prefer to combine into a linear O–Cu–O structure [Fig. 10(b)], which improves the Cu adsorption energy to −2.77 eV (i.e., 0.04 eV more stable than Cu on the nonoxidized surface). In this cluster, the oxygen adatoms are positioned slightly offset from two nearest fcc sites and the Cu adatom is located roughly in the middle between an hcp and a top site. Note that this adsorption energy is calculated with reference to a 2/9-ML oxidized surface in which the two oxygen adatoms are in a separated configuration. This is to say the energy penalty for bringing two oxygen adatoms together into nearest fcc sites in order to form the O–Cu–O cluster is included in the adsorption energy. Assuming the two oxygen adatoms to be already at the nearest sites improves the Cu adsorption energy in the linear O–Cu–O cluster to a more favorable −3.14 eV; in this sense, Cu adsorption can be seen as stabilizing an unfavorably dense oxygen adatom arrangement.

We have similarly examined Cu adsorption on a ZnO(0001) surface which is oxidized by a 1/9-ML coverage of zinc vacancies. Using a (3×3) supercell of ZnO(0001), we find that the Cu adatom prefers the fcc site that is furthest from the zinc vacancy. In this configuration, the Cu adsorption energy evaluates to −2.49 eV, which is 0.23 eV less stable than the same Cu coverage on the bulklike (i.e., nonoxidized) surface, but slightly (0.08 eV) more stable than adatom-oxidized surface. We have also tested whether it would be advantageous for the Cu adatom to fill the Zn vacancy site, thus, in effect, becoming a substitutional Cu atom. We find that this vacancy-filling configuration is slightly (0.04 eV) less stable than the aforementioned configuration where Cu adatoms and Zn vacancies are separated. This somewhat counterintuitive result reverses when we consider a 1/4-ML coverage of zinc vacancies in a (2×2) unit cell. In this case, the adsorption energy for a vacancy-filling Cu atom evaluates to −2.78 eV, which is 0.30 eV more stable than a 1/4-ML coverage of Cu_{fcc} adatoms on the bulklike surface. At 1/4-ML coverage, the vacancy-filling Cu atom is also considerably more stable (by 1.95 eV) than a separated zinc vacancy and Cu_{fcc} adatom.

Other authors have looked at the binding of Cu atoms at a zinc vacancy site, reporting adsorption energies of −2.00 eV (Ref. 22), −3.10 eV (Ref. 26), and −2.97 eV (Ref. 27) at various levels of theory.[62] These results all come from cluster model calculations, which raises the question to what vacancy coverage these results correspond to. Since typical cluster models impose charge neutrality on a rather localized level, we believe they are best compared to a 1/4-ML vacancy coverage [i.e., a stoichiometric, $\Gamma_O = 0$ ZnO(0001) surface; cf. Sec. II E]. Our Cu adsorption energy of −2.78 eV at 1/4 ML is thus in reasonable agreement with these earlier results.

Last, we explore the effect of weak surface oxidation on the stability of Cu(111) overlayers, using a single monolayer of Cu(111) and the (4×4):(3×3) lattice match discussed in the previous section. This system was oxidized to a level of 1/9 ML, using either a surface zinc vacancy, or an extra oxygen atom. For the position of the latter, three different sites were tested, namely, a top and a fcc site relative to the ZnO(0001) substrate *below* the Cu(111) monolayer, as well as an fcc site *above* the Cu(111) monolayer. Of the four cases,

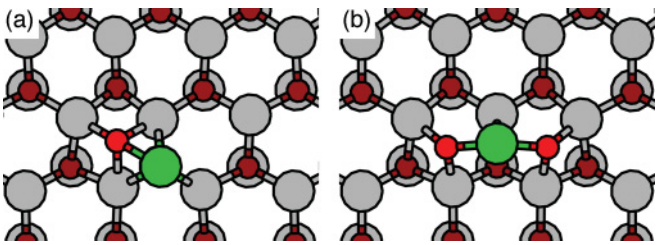

FIG. 10. (Color online) Top-view of the linear (a) CuO and (b) CuO_2 admolecules on the bulklike ZnO(0001) surface. These structures arise as favored geometries through the attraction between Cu and O adatoms.

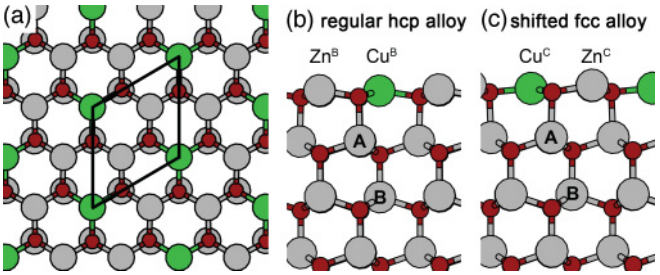

FIG. 11. (Color online) Surface alloy phases on ZnO(0001). (a),(b) Top and side views, respectively, of a 1/3-ML Cu surface alloy. This structure was proposed in Ref. 18 as a model for the experimentally observed $(\sqrt{3}\times\sqrt{3})$R30° LEED pattern and is described by the regular hcp stacking sequence $[Cu^{B}_{1/3}Zn^{B}_{2/3}]O^{A}Zn^{A}O^{B}Zn^{B}\cdots$. (c) Side view of a 1/3-ML shifted alloy structure in which the Cu/Zn plane is shifted to an fcc registry (i.e., site C); that is, the stacking sequence is $[Cu^{C}_{1/3}Zn^{C}_{2/3}]O^{A}Zn^{A}O^{B}Zn^{B}\cdots$. Zinc, copper, and oxygen atoms are represented by the large pale gray, large dark gray (green), and small (red) circles, respectively.

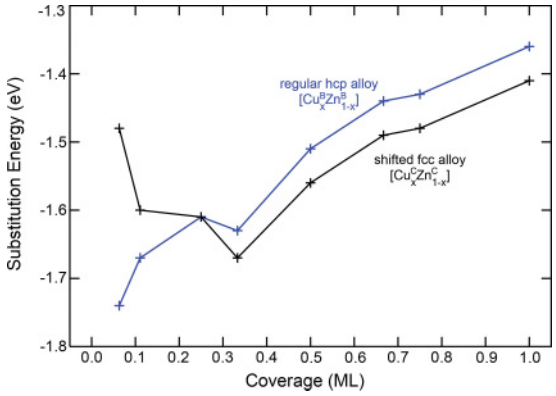

FIG. 12. (Color online) Calculated Cu substitution energies for the nonreconstructed ZnO(0001) surface as a function of substitution coverage. Shown are substitution energies for the surface $[Cu_xZn_{1-x}]$ plane adopting the regular hcp (i.e., site B) and the shifted fcc (site C) registry (cf. Fig. 11).

the configuration with an oxygen atom at a fcc site *above* the Cu(111) monolayer is preferred, having the lowest surface free energy. For this 1/9-ML oxidized structure the average per-Cu-atom adsorption energy evaluates to −3.22 eV, to be compared with −3.31 eV for the same overlayer on bulklike ZnO(0001). Note, however, that these small differences are primarily a reflection of the large number of Cu atoms in the unit cell that are affected by the addition of a single oxygen atom. Collectively, the adhesion of the Cu overlayer is made 1.51 eV less stable by the addition of the oxygen atom.

An important concluding observation for these *mildly* oxidized ($\Gamma_O = 0$ and below) ZnO(0001) surfaces is that the calculated Cu adsorption energies remain significantly smaller than the bulk Cu cohesive energy in *all* considered cases. This is to say Cu atoms under these conditions will prefer to exist in the form of bulk copper instead of attaching themselves to the ZnO(0001) surface as adatoms or Zn-vacancy-filling (i.e., substitutional) Cu atoms. As we show in the following sections, higher levels of surface oxidation, implying denser packings of substitutional Cu atoms, will be required to render such structures thermodynamically stable.

E. Substitutional Cu in bulklike ZnO(0001)

In this section we consider alloy structures in which copper atoms substitute for zinc in the clean ZnO(0001) surface. An illustrative example of this structure type is shown in Figs. 11(a) and 11(b). We compare here the thermodynamic stability of various surface structures of the general form $[Cu^{B}_{x}Zn^{B}_{1-x}]O^{A}Zn^{A}O^{B}\cdots$ using substitution energies and phase stability diagrams.

Copper substitution energies are calculated using the expression

$$E_{\rm sub} = \frac{1}{n}[\Delta E_{\rm slab} + n(E_{\rm Zn(atom)} - E_{\rm Cu(atom)})], \qquad (20)$$

where $\Delta E_{\rm slab} = E_{\rm alloy} - E_{\rm ZnO(0001)}$ is the energy difference between a clean bulklike slab and an alloy slab of the same size. The energy of free atoms is denoted $E_{\rm Zn(atom)}$ and $E_{\rm Cu(atom)}$, and n is the number of Cu substitutions in the slab.

The data in Fig. 12 show that the substitution energies are negative across the coverage range, becoming less favorable with Cu content. At 1/16 ML, the substitution energy evaluates to −1.74 eV to be compared with −1.36 eV for a full monolayer, which indicates some form of repulsion between the substituting Cu atoms. An interesting observation is made when we shift the alloyed atomic layer at the surface from the B site to the C site, that is, from an hcp to an fcc stacking [see illustration in Fig. 11(c)]. At low Cu content (<1/4 ML) this shift leads to less favorable substitution energies. The regular hcp registry is slightly preferred for the clean ZnO(0001) surface plane by about $\Delta E_{\rm shift} = 0.015$ eV per (1×1) unit and this preference asserts itself at very low Cu coverages. Note how the adsorption energy for the shifted alloy swings sharply upward to less stable substitution energies as the coverage is reduced, in line with an expected $\propto\Delta E_{\rm shift}/\theta$ dependence in the limit of low coverage θ. However, at approximately 1/3 ML and above, the shifted fcc registry of the surface plane is favored by about 0.05 eV per Cu atom. The energy data in Fig. 12 illustrate the switch in preference from a regular (hcp) to a shifted (fcc) configuration.

In trial calculations for 1/3, 2/3, and 1 ML, we have confirmed that Cu substitution in the second (i.e., subsurface) zinc layer is less favorable by 0.17, 0.32, and 0.35 eV, respectively; thus, we can rule out subsurface alloys as viable surface phases. Any substitutional Cu in the subsurface would be expected to segregate to the surface.

The stability of these alloy phases relative to the clean, bulklike surface is assessed using the one-dimensional phase stability diagram in Fig. 13(a). Included in this graph and plotted against the Cu chemical potential are alloy phases for all the Cu coverages considered in this work, though we have limited the display to only the most stable registry (regular or shifted) for a given coverage. Shown in solid thick (red) lines is the resultant minimum free-energy curve for the alloy phases, showing a clear transition from the bulklike ZnO(0001) surface at low $\Delta\tilde{\mu}_{\rm Cu}$ to a full 1-ML Cu alloy phase at high $\Delta\tilde{\mu}_{\rm Cu}$. In between, 1/3- and 2/3-ML Cu alloys are briefly stable. This transition occurs at negative $\Delta\tilde{\mu}_{\rm Cu}$, which means that the alloy

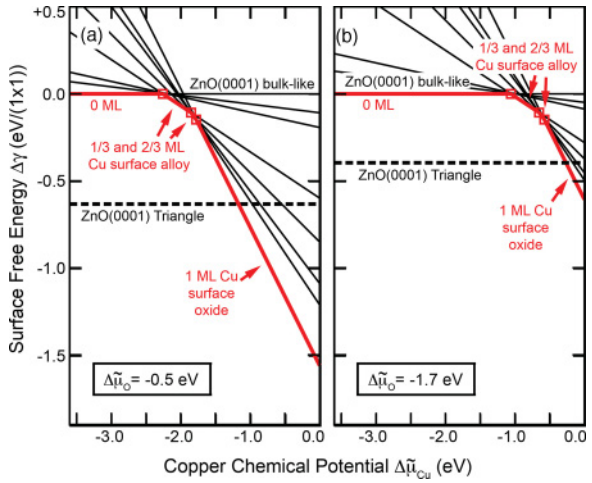

FIG. 13. (Color online) Phase stability diagram for the alloy phases of the clean ZnO(0001) surface. Panels (a) and (b) show the free energies for an oxygen chemical potential, $\Delta\tilde{\mu}_O$, of -0.5 and -1.7 eV, respectively.

phases become favored over bulklike ZnO(0001) prior to the onset of bulk Cu precipitation.

These results make sense when considered in terms of Cu atom adsorption energies to fill a preexisting coverage of zinc vacancies. As discussed in the previous section, at low Zn vacancy densities of 1/9 and 1/4 ML, the calculated Cu adsorption energies for filling these vacancies are -2.45 and -2.78 eV, respectively, and thus significantly less stable than the bulk copper cohesive energy of -3.49 eV. The situation changes at higher vacancy densities: At 1/3 ML, the Cu adsorption energy evaluates to -3.72 eV and is thus more stable than bulk copper. At even higher coverages of 2/3 and 1 ML, the adsorption energy increases drastically to -5.51 and -6.19 eV.

However, the stability of these alloys over the bulklike surface is not enough. As we have discussed in Sec. III B, the bulklike ZnO(0001) surface itself is unstable against the oxidized surface phases. Depending on $\Delta\tilde{\mu}_O$, the preferred oxidized ZnO reconstruction is between 0.08 and 0.79 eV/(1 × 1) more stable than bulklike ZnO(0001). An additional complication arises because the free energy of the alloy phases is also dependent on the oxygen chemical potential through the third and fourth term in Eq. (3).[63] A comparison of Figs. 13(a) and 13(b), plotted for oxygen chemical potentials -0.5 and -1.7 eV, respectively, illustrates that a more negative $\Delta\tilde{\mu}_O$ results in a uniform shift of the alloy phase lines to the right (i.e., the transitions occur at a less negative $\Delta\tilde{\mu}_{Cu}$). This means that the formation of alloy phases is favored by more oxidizing conditions. Inserted into these two graphs as horizontal dashed lines are the surface free energies of the preferred oxidized ZnO(0001) phase at the respective $\Delta\tilde{\mu}_O$. Relative to this oxidized ZnO surface, only the full monolayer (shifted) alloy phase is stable, provided $\Delta\tilde{\mu}_{Cu}$ is sufficiently large.

Shown in Figs. 14(a) and 14(b), the structure of this stable Cu phase is characterized by a $(\sqrt{3}\times\sqrt{3})$R30° unit cell and a monolayer of Cu atoms. In the top view [Fig. 14(a)] it can be seen that the Cu atoms have relaxed away from a high-symmetry fcc position to form equilateral Cu_3 triangles. With a Cu-Cu distance of 2.72 Å, these triangles are not dissimilar

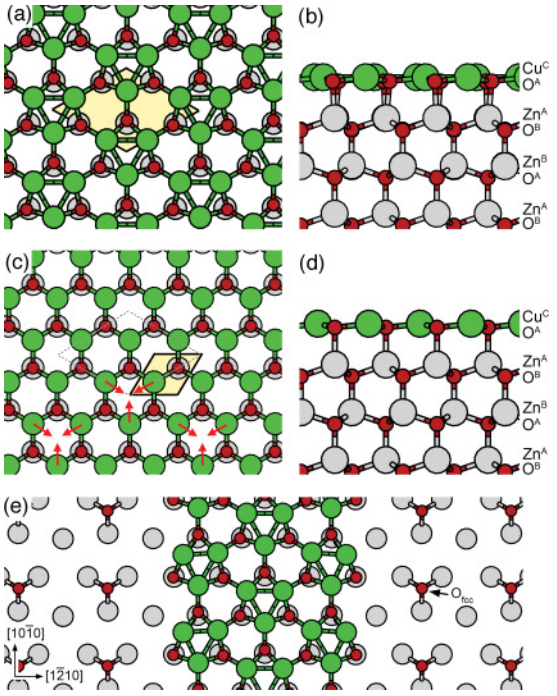

FIG. 14. (Color online) (a),(b) Top and side views, respectively, of the $(\sqrt{3}\times\sqrt{3})$R30° Cu_4O_3-ZnO(0001) thin copper oxide overlayer structure on ZnO(0001). This phase is described by a $Cu^CO^AZn^AO^BZn^B\cdots$ stacking sequence and it appears as a stable surface phase in the upper center part of our two-dimensional phase diagram in Fig. 2. The structure can be though of as arising from a high-symmetry (1 × 1) variant shown in panels (c) and (d). As indicated by arrows in panel (c), copper atoms in sets of three relax away from the high-symmetry fcc site to form the characteristic Cu_3 trimers of the broken-symmetry $(\sqrt{3}\times\sqrt{3})$R30° phase. Panel (e) shows a plausible geometry for a phase boundary between Cu_4O_3-ZnO(0001) (in the center) and 2/9-ML O_{fcc} oxidized ZnO(0001) (left and right). Only the three surface-nearest atomic layers (Cu, O, and Zn) are shown in the top-view panels (a), (c), and (e).

to the Cu adatom trimer structures discussed in Sec. III C. The key difference here is that these trimers are linked to the bulklike ZnO(0001) surface via a full monolayer of oxygen atoms. With a nominal overlayer stoichiometry of $Cu_1O_{3/4}$, or Cu_4O_3 (note: one-quarter of the oxygen monolayer is attributed to the ZnO substrate; see discussion in Sec. II E), this phase is referred to more appropriately as a copper oxide overlayer phase. Labeled Cu_4O_3-ZnO(0001) in the following, this phase appears prominently in our two-dimensional phase diagram (see Fig. 2), giving rise to the upper left portion of the (red-shaded) CuO_x overlayer phase region.

In terms of our simplified stacking notation, this Cu_4O_3 phase is described as $Cu^CO^AZn^AO^BZn^B\cdots$. This notation captures the layer stacking/stoichiometry; however, it idealizes the in-plane relaxations away from the fcc site (i.e., the C site) that leads to the Cu_3 triangles. In fact, we can describe the $(\sqrt{3}\times\sqrt{3})$R30° phase as a symmetry-breaking (Jahn-Teller) distortion arising from a high-symmetry (1 × 1) variant in which the Cu atoms are in-plane constrained to the fcc site. Shown in Figs. 14(c) and 14(d), this (1 × 1) variant is calculated to be marginally less stable than the $(\sqrt{3}\times\sqrt{3})$R30° by about 0.02 eV per Cu triangle, which

suggests that the (1×1) structure itself is not a stable energy minimum. The calculated energy difference is very small indeed; however, various accuracy tests[64] suggest that this result is genuine and significant, at least within a GGA-DFT formalism. Contributing to the relative stability of the $(\sqrt{3} \times \sqrt{3})$R30° phase over the (1×1) phase is the fact that the former maintains a finite spin magnetic moment in the Cu_4O_3 overlayer (1.51 μ_B per Cu_3 triangle), while the latter does not.[65]

It should be noted that any Cu atom in the high-symmetry (1×1) phase is surrounded by three vacant fcc sites, and hence, there exist three degenerate ways by which Cu atoms can distort into Cu_3 triangles and a $(\sqrt{3} \times \sqrt{3})$R30° phase. Given the small energy difference between (1×1) and $(\sqrt{3} \times \sqrt{3})$R30°, it is thus likely that the $(\sqrt{3} \times \sqrt{3})$R30° phase can thermally average over these degenerate configurations and give rise to a net (1×1) appearance in experiment. However, there are two circumstances which could lead to a stable and observable $(\sqrt{3} \times \sqrt{3})$R30° reconstruction. First, the relaxation of Cu atoms into triangles is highly correlated through the second, oxygen atomic plane. This becomes evident, for instance, in the position of these oxygen atoms relative to the zinc atoms in the third layer. We see, for example, in Fig. 14(c) that the second-layer oxygen atoms in the (1×1) structure are centered directly above the zinc atoms. This is in contrast to the $(\sqrt{3} \times \sqrt{3})$R30° structure [Fig. 14(a)], where the oxygen atoms are clearly shifted off center, in line with the displacements of Cu atoms into triangles. This implies that Cu atoms can shift between degenerate triangle configurations only in concert with all the other Cu atoms in the surface which would significantly enhance the activation barriers involved. In addition, step edges and phase boundaries are likely to break the degeneracy, as Cu atoms at such edges will have fewer options to relax into Cu_3 triangles. This is illustrated in Fig. 14(e), showing a plausible geometry for a step edge/phase boundary between Cu_4O_3-ZnO(0001) (in the center) and a partially O_{fcc}-oxidized ZnO(0001) surface (left and right). The particular phase boundary shown here runs parallel to the $[10\bar{1}0]$ axis of ZnO(0001), the edge is nonpolar (edge-geometry is the same on both sides), and it maintains the stoichiometry of two phases involved. Most importantly, we see that there is only a single mode for the edge-nearest Cu atoms to relax into a Cu_3 pattern, which in turn locks other Cu atoms into a stable $(\sqrt{3} \times \sqrt{3})$R30° pattern.

We acknowledge in passing that the (1×1) Cu_4O_3-ZnO(0001) high-symmetry structure was identified earlier by Dai *et al.*[29] as the most favorable site permutation of 1 ML of Cu and 1 ML of oxygen on ZnO(0001). However, these authors did not consider symmetry breaking into a more stable $(\sqrt{3} \times \sqrt{3})$R30° form, nor did they establish the thermodynamic stability of these structures over other stoichiometries, including bulklike and oxidized ZnO(0001), or bulk copper/copper oxide. In this regard we improve on this earlier work by showing that the $(\sqrt{3} \times \sqrt{3})$R30° Cu_4O_3-ZnO(0001) phase is a minimum free-energy reconstruction within the allowed $\Delta\tilde{\mu}_O$,$\Delta\tilde{\mu}_{Cu}$ space. Hence, this phase should be observable in experiment, most likely with (1×1) symmetry arising from thermal averaging over degenerate $(\sqrt{3} \times \sqrt{3})$R30° configurations, and possibly with $(\sqrt{3} \times \sqrt{3})$R30° symmetry in a sample rich in step edges and phase boundaries. This distinction will be of some relevance when we later discuss the experimental evidence for this phase.

F. Substitutional Cu in oxidized ZnO(0001)

The existence of the Cu_4O_3-ZnO(0001) surface motivates us to explore Cu substitution in some of the oxidized ZnO surface phases. The size of the triangular pit structures prevents us from systematically examining Cu substitution in these structures. Instead, we focus our attention on the simple oxygen adatom and Zn-vacancy structures and examine if, and under what conditions, Cu substitution leads to stable reconstruction.

Specifically, we have substituted Zn for Cu atom-for-atom in the (2×2) 1/4-ML O_{fcc} structure to create a set of 1/4-ML oxidized alloy structures containing between 0 and 1 ML Cu. As in the previous section, we consider both the regular (site B) and shifted (site C) registry of the $[Cu_xZn_{1-x}]$ atomic plane. Note that the oxygen adatoms are shifted with the cation plane so as to retain their fcc positioning. The same procedure was applied to create alloy phases for the 1/3-ML $(\sqrt{3} \times \sqrt{3})$R30° oxygen adatom and the 1/4-ML (2×2) Zn-vacancy phases.

The most interesting results are obtained for the set of alloys with 1/3-ML O_{fcc} adatoms. The phase stability diagram for this set is shown in Fig. 15(a), comparing the alloys between 0-ML and 1-ML Cu, assuming an oxygen chemical potential of -0.5 eV. The resultant minimum free-energy curve of the 1/3-ML O_{fcc} alloy is shown in thick (blue) lines and is

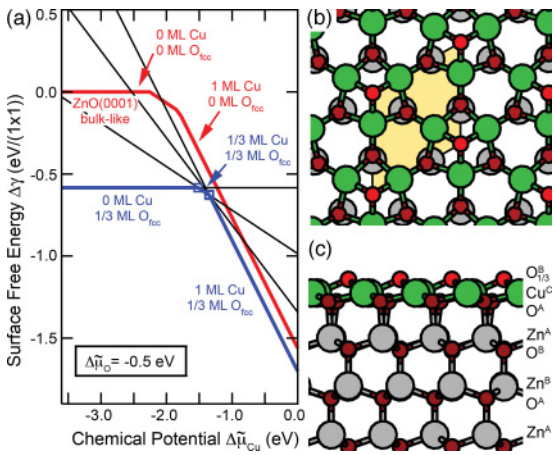

FIG. 15. (Color online) (a) Phase stability of copper alloy phases of the oxidized ZnO(0001) surface. Shown as a thick (red) curve is the minimum free energy for Cu substitution in a surface oxidized with 1/3-ML oxygen adatoms (O_{fcc}). Included for comparison is the free-energy curve for alloys of the clean (nonoxidized) surface taken from Fig. 13. (b),(c) Top and side views, respectively, of the very stable 1-ML Cu and 1/3-ML O_{fcc} copper oxide overlayer structure with a $(\sqrt{3} \times \sqrt{3})$R30° unit cell. The stacking sequence of this structure is described as $O^B_{1/3}Cu^CO^AZn^AO^BZn^B\cdots$. This structure with an overlayer stoichiometry of $Cu_{12}O_{13}$ appears as a stable phase in our two-dimensional phase diagram Fig. 2.

compared to that of the clean surface alloys (thick red line) taken from Fig. 13(a). Across the $\Delta\tilde{\mu}_{Cu}$ range, the oxidized phases are more stable, and at approximately -1.4 eV, the Cu-free, oxidized ZnO(0001) surface transitions into a 1-ML Cu, 1/3-ML O_{fcc} phase. In a very narrow $\Delta\tilde{\mu}_{Cu}$ window, the shifted 1/3- and 2/3-ML Cu phases are stable (between -1.51 and -1.34 eV and between -1.34 and -1.35 eV, respectively); broadly speaking, however, the transition is quite sharp between the Cu-free and the full monolayer phase.

A more negative oxygen chemical potential would shift the free-energy curve of the oxidized alloy relative to that of the clean surface alloy, such that at $\Delta\tilde{\mu}_O < -1.0$ eV, the nonoxidized 1-ML Cu structure becomes preferred over the 1/3-ML oxidized one. These two phases are in prominent competition in our two-dimensional phase diagram (Fig. 2) and together constitute the bulk of the Cu-oxide overlayer phase region. The 1/3-ML alloy, and marginally the 2/3 ML, carve out a small region of stability between the 1-ML Cu phases and the Cu-free ZnO(0001) surface reconstructions.

For the 1/4-ML O_{fcc} and the 1/4-ML Zn-vacancy sets of alloys, the qualitative shape of the minimum free-energy curves is analogous to those of the clean surface and 1/3-ML O_{fcc} alloys in Fig. 15(a); however, neither set gives rise to Cu-containing phases that are thermodynamically stable against either the 0-ML or the 1/3-ML O_{fcc} phase at any $\Delta\tilde{\mu}_O$. None of the structures from these two sets appears in the two-dimensional phase diagram (Fig. 2).

The structure of the 1-ML Cu, 1/3-ML O_{fcc} $(\sqrt{3}\times\sqrt{3})R30^\circ$ phase is shown in Figs. 15(b) and 15(c) and is characterized by a $O^B_{1/3}Cu^CO^AZn^AO^BZn^B\cdots$ stacking sequence. Thus, this phase differs from the Cu_4O_3-ZnO(0001) phase only by the addition of 1/3-ML oxygen adatoms. These adatoms decorate all of the Cu_3 trimers of the Cu_4O_3 phase which results in a considerable expansion of the Cu–Cu bond distance from 2.72 to 3.47 Å. The stoichiometry of this copper oxide overlayer (see Sec. II E) evaluates to $CuO_{1/3+1-1/4}$ or $Cu_{12}O_{13}$. The net magnetic moment in the $Cu_{12}O_{13}$ overlayer evaluates to 0.54 μ_B per Cu_3 triangle, which is considerably reduced from the 1.49 μ_B found for the Cu_4O_3-ZnO(0001) phase.

G. Oxygen adatoms on Cu_4O_3-ZnO(0001)

Our survey of alloy structures in the previous section identified two stable copper oxide overlayer phases that reconstruct with a $(\sqrt{3}\times\sqrt{3})R30^\circ$ unit cell; the first with a Cu_4O_3 and the second with a $Cu_{12}O_{13}$ overlayer stoichiometry. The latter is distinguished from the former by the addition of 1/3-ML oxygen adatoms at the fcc site. In this section we examine whether other oxygen adatom coverages on Cu_4O_3-ZnO(0001) are thermodynamically stable. We geometry-optimize copper oxide overlayer structures of the general pattern $O^B_xCu^CO^AZn^AO^B\cdots$ with the adatom coverage ranging from 1/16 to 1 ML using unit cells of up to (4×4) in size. For coverages of 1/3, 2/3, and 1 ML we have verified that the fcc site (i.e., site B in the stacking sequence above) is the preferred position of oxygen adatoms on Cu_4O_3-ZnO(0001).

Figure 16 plots the calculated oxygen adsorption energies on Cu_4O_3-ZnO(0001) as a function of adatom coverage. These energies are calculated analogous to Eq. (16) and are referenced to the energy of molecular oxygen and

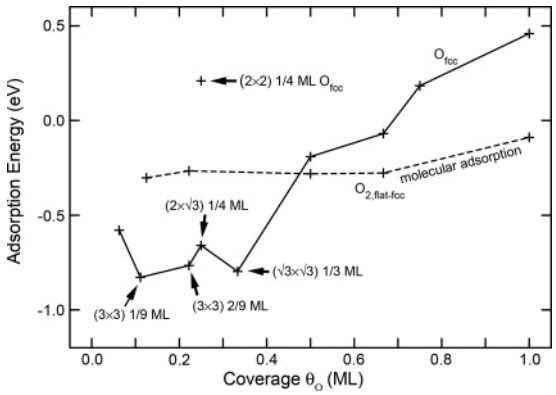

FIG. 16. Calculated oxygen adsorption energies on the Cu_4O_3-ZnO(0001) surface as a function of coverage. Plotted are fcc oxygen adatoms and flat-fcc molecular adsorbates which are connected using solid and dashed lines, respectively. Adsorption energies are reported relative to the $(\sqrt{3}\times\sqrt{3})R30^\circ$ phase of Cu_4O_3-ZnO(0001).

the $(\sqrt{3}\times\sqrt{3})R30^\circ$ reconstructed Cu_4O_3-ZnO(0001) phase. Qualitatively, the adsorption energies are considerably smaller than those for the bulklike ZnO(0001) surface (cf. Fig. 3). For example, for the two most stable coverages of 1/9 and 1/3 ML the adsorption energies evaluate to -0.83 and -0.80 eV, respectively, to be compared with -3.50 and -2.17 eV on bulklike ZnO(0001). Above a coverage of 1/3 ML, the adsorption energy becomes sharply less negative, indicating a repulsive interaction between the oxygen adatoms as similarly found on bulklike ZnO(0001). At coverages below 1/3 ML, the adsorption energies are sensitively dependent on the coverage and surface unit cell used. The data show that $(\sqrt{3}\times\sqrt{3})R30^\circ$ (at 1/3 ML) and (3×3) unit cells (at 1/9 and 2/9 ML) are significantly preferred over (2×2) 1/4-ML, (4×4) 1/16-ML, and $(2\times\sqrt{3}R30^\circ)$ 1/4-ML unit cells. This can be rationalized in terms of the surface relaxations that give rise to the Cu_3 trimers in the $(\sqrt{3}\times\sqrt{3})R30^\circ$ Cu_4O_3- and $Cu_{12}O_{13}$-ZnO(0001) phases [Figs. 14(a) and 14(b) and 15(a), respectively]: Unit cells that are not supercells of $(\sqrt{3}\times\sqrt{3})R30^\circ$ are restricted in their ability to form such trimers. In consequence, the associated oxygen coverages are less stable.

We have also considered several configurations and coverages of molecularly adsorbed oxygen. As on the bulklike ZnO(0001) surface, we find that the flat-fcc adsorption geometry is preferred on Cu_4O_3-ZnO(0001). The coverage-dependent adsorption of this configuration is included in Fig. 16 as a dashed curve. We see that in qualitative terms, the energetics of molecularly adsorbed oxygen on Cu_4O_3-ZnO(0001) closely matches that of bulklike ZnO(0001). In comparison to oxygen adatoms, the energetics of molecularly adsorbed oxygen is much less coverage-dependent such that there is a crossover in preference at a coverage, θ_O, of approximately 1/2 ML.

The phase stability of oxygen adatom and admolecule structures is compared in Fig. 17. This comparison is best made along a diagonal in $(\Delta\tilde{\mu}_O;\Delta\tilde{\mu}_{Cu})$ space, running from $(-1.7\,eV; 0.0\,eV)$ to $(0.0\,eV; -1.7\,eV)$, and thus entirely within a regime where copper oxide overlayer phases are stable (cf.

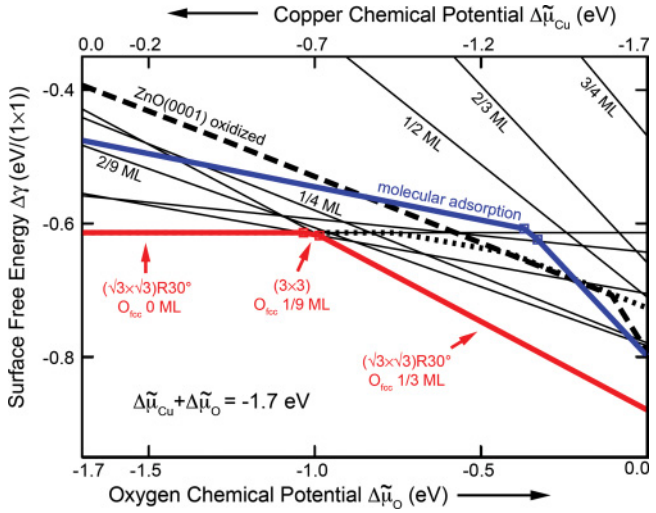

FIG. 17. (Color online) Phase stability diagram comparing oxygen adatom structures on the Cu_4O_3-ZnO(0001) surface. The diagram is plotted along a diagonal in $\Delta\mu_O$, $\Delta\mu_{Cu}$ space such that the two chemical potentials are linked as indicated by the equation shown. The minimum free-energy curve [thick solid (red) lines] shows that there are only three stable oxygen adatom coverage on this surface, namely $(\sqrt{3}\times\sqrt{3})$R30° 0 ML and 1/3 ML as well as (3×3) 1/9 ML, with many other coverages not stable. The dotted and dashed minimum free-energy curves indicates for reference, the relative energy of Cu vacancy structures and the ZnO triangle reconstructions.

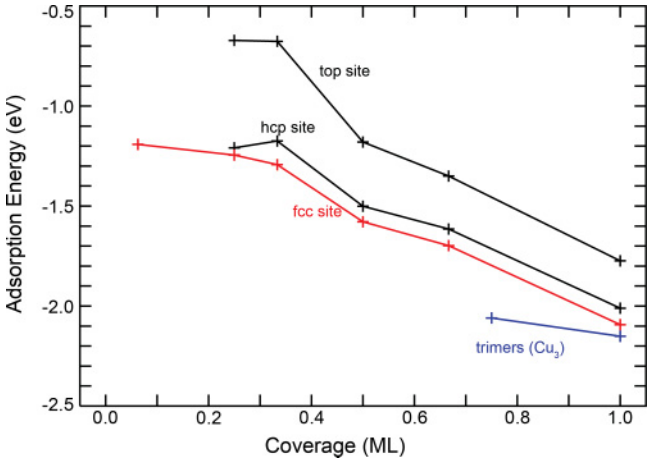

FIG. 18. (Color online) The adsorption energy of Cu atoms (in eV per atom, relative to free Cu atoms) on the Cu_4O_3-ZnO(0001) surface as a function of coverage. Shown are the adsorption energies for single atoms at the high-symmetry fcc, hcp, and top sites. Also included are Cu_3 adatom clusters at 3/4 and 1 ML. Adsorption energies are relative to the $(\sqrt{3}\times\sqrt{3})$R30° phase of Cu_4O_3-ZnO(0001).

the two-dimensional phase diagram Fig. 2). Included in Fig. 17 as thin solid lines are all the fcc-oxygen adatom structures considered, ranging from 1/16 to 1 ML. The minimum free-energy curve [thick solid (red) curve] shows that only three phases are stable, namely, 0 ML $(\sqrt{3}\times\sqrt{3})$R30°, 1/9 ML (3×3), and 1/3 ML $(\sqrt{3}\times\sqrt{3})$R30°, with phase transitions at oxygen chemical potentials of −1.03 and −0.99 eV. Other adatom coverages do not appear as stable phases anywhere in the phase diagram and the 1/9-ML phase is limited to a very narrow window of stability which suggests a very sharp transition between the adatom-free Cu_4O_3-ZnO(0001) surface and the 1/3-ML phase, that is, the $Cu_{12}O_{13}$-ZnO(0001) surface discussed in the previous section. Such a sharp transition is likely to become manifest in a strong ordering of any oxygen adatoms on Cu_3O_4-ZnO(0001) into local 1/3-ML islands.

The minimum free-energy curve for the molecular oxygen adsorbates is shown as a thick solid (blue) line in Fig. 17. We see that across the entire chemical potential range, the molecular adsorbate phase is less favorable than the adatom structures. Therefore, molecular adsorbate structures of oxygen on Cu_4O_3-ZnO(0001) do not occur as stable phases in our two-dimensional phase diagram (Fig. 2).

Also indicated for reference in Fig. 17 are the minimum free-energy curves for Cu-vacancies on Cu_4O_3-ZnO(0001) (thick dotted curve) and the Cu-free oxidized ZnO(0001) surface (thick dashed line; cf. Fig. 5). The data show that Cu vacancies are not an effective mechanism to oxidize the Cu_4O_3-ZnO(0001) surface, with their free energies always less stable than the preferred oxygen adatom structure. The free-energy curve of the oxidized ZnO(0001) phases in Fig. 17 (i.e., triangular pits and oxygen adatoms; curve taken from Fig. 5) is also above the curve of the copper oxide overlayers, and thus the latter phases are more stable along the chemical potential diagonal plotted. Shifting of this diagonal to a more negative $\Delta\tilde{\mu}_{Cu}$ shifts the copper oxide overlayer and the oxidized ZnO(0001) free-energy curves relative to each other. Eventually, at a sufficiently negative $\Delta\tilde{\mu}_{Cu}$, the oxidized ZnO(0001) phases become preferred.

H. Copper adsorption on Cu_4O_3-ZnO(0001)

Next we consider whether copper adsorption on the Cu_4O_3-ZnO(0001) structure (Fig. 14) leads to any stable surface phases. Plotted in Fig. 18 are the calculated adsorption energies of Cu atoms at the fcc, hcp, and top sites for coverages between 1/16 and 1 ML. Over this range, we find that Cu adatoms prefer the fcc site over the hcp and top site. In comparison to the bulklike ZnO(0001) surface (see data in Fig. 7), the adsorption energies on Cu_4O_3-ZnO(0001) are generally smaller across the coverage range. Similar between the two surfaces, however, is the pattern that the adsorption energy becomes more negative (i.e., more stable) toward higher coverage, indicative of an attraction between Cu adatoms in this regime. As a result, the highest adsorption energies for Cu_4O_3-ZnO(0001) occur at high coverage. A full monolayer of Cu adatoms at the high-symmetry fcc site has an adsorption energy of −2.09 eV per atom, to be compared with −2.65 eV for the bulklike ZnO(0001) surface.

As on the bulklike surface, the apparent attraction above 1/3 ML is associated with Cu adatoms being positioned at adjacent sites. Further stabilization is thus again achieved by the formation of adatom trimer clusters (Cu_3) in which the Cu atoms are displaced from the high-symmetry position toward the Cu atoms at the adjacent site such that Cu–Cu bonds can be formed. Trimerization into Cu_3 clusters in a $(\sqrt{3}\times\sqrt{3})$R30° unit cell slightly improves the adsorption energy for 1-ML Cu to −2.15 eV.

TABLE VIII. Calculated copper binding energies (in eV per atom, relative to free Cu atoms) for various monolayer (ML) coverages and superlattice matchings of a Cu(111) overlayer on a Cu_4O_3-ZnO(0001) substrate. The superlattice mismatch, μ, is also reported based on the calculated lattice constants of 2.579 and 3.289 Å for bulk Cu(111) and ZnO(0001), respectively.

Cu	:	Cu_4O_3-ZnO	μ (%)	1 ML (eV)	2 ML (eV)	3 ML (eV)	4 ML (eV)	5 ML (eV)
(1×1)	:	(1×1)	−22	−2.09	−2.65	—	—	—
(4×4)	:	(3×3)	+5	−2.97	−3.16	−3.25	−3.30	−3.33

Two monolayers of Cu on Cu_4O_3-ZnO(0001) with a (1×1) repeat have the preferred stacking $Cu^CCu^BCu^CO^AZn^AO^B \cdots$ and thus prefer the second monolayer to be hcp stacked over the first monolayer at the fcc position. This is again analogous to the clean ZnO(0001) surface (see Sec. III C) for which 2-ML Cu atoms were found to adopt the same relative in-plane registry of the Cu monolayer. The calculated adsorption energies are summarized in Table VIII. For 2-ML copper (1×1) on Cu_4O_3-ZnO(0001) (1×1) the adsorption energy evaluates to −2.65 eV, which is considerably more stable than any of the single adatom or Cu_3 cluster structures discussed above.

As on the bulklike ZnO(0001) surface, the most stable adsorption energies on Cu_4O_3-ZnO(0001) are achieved when the Cu overlayers are lattice matched to the substrate. A single Cu(111) atomic layer with a (4×4) repeat is matched with a (3×3) supercell of Cu_4O_3-ZnO(0001) for an average copper adsorption energy of −2.97 eV per Cu atom. This adsorption energy gradually improves as further Cu(111) layers are added, reaching a value of −3.33 eV for the thickest overlayer considered [five layers of Cu(111)].

Overall, the Cu adsorption energies on Cu_4O_3-ZnO(0001), irrespective of adsorption geometry, are found to be less stable than on the clean ZnO(0001) surface. The adsorption energies are also significantly less stable than the calculated formation energy of bulk Cu (−3.49 eV) and only come close to this value as the Cu overlayer becomes increasingly bulk-like. As a result, none of the Cu adatom surface structures is thermodynamically stable anywhere in the allowable $\Delta\tilde{\mu}_O$, $\Delta\tilde{\mu}_{Cu}$ chemical potential space. For the Cu adsorption structures considered in this section, the formation of bulk Cu (at $\Delta\tilde{\mu}_{Cu} > 0$ eV) will always be preferable.

I. Cu_2O-like overlayers on bulklike ZnO(0001) and Cu_4O_3-ZnO(0001)

Alternative structure models advanced in the literature[21,66] for a copper-oxide overlayer on ZnO(0001) take inspiration from the crystal structure of bulk cuprous oxide, Cu_2O, shown in Fig. 19. There are two plausible orientations of Cu_2O on ZnO(0001), namely, $[111]_{Cu_2O} \| [0001]_{ZnO}$ and $[110]_{Cu_2O} \| [0001]_{ZnO}$. We examine in this section how these "Cu_2O(111)-like" and "Cu_2O(110)-like" overlayer structures compare in stability to the Cu_4O_3- and $Cu_{12}O_{13}$-ZnO(0001) phases identified in the previous sections.

Cu_2O(111)-like overlayers. Along the [111] direction, the Cu_2O lattice is conveniently thought of as a stacking of Cu_2O_4 *trilayer* structural elements as illustrated in Fig. 19(b). Shown in top and side views in Figs. 19(c) and 19(d), respectively, a single trilayer is composed of a single hexagonal plane of Cu atoms, with two 1/4-ML planes of oxygen atoms above and below. All but one of the Cu atoms in the trilayer unit cell are linearly coordinated by oxygen atoms that belong to the trilayer. The one remaining Cu atom is referred to as coordinatively unsaturated (CUS), or simply as Cu_{CUS}. In bulk, this Cu atom is coordinated by the oxygen atoms of adjacent trilayers; however, in an isolated trilayer, or when exposed at a surface, this type of Cu atom is undercoordinated and predicted[51] to be absent.

The in-plane hexagonal repeat length of a trilayer is calculated to be $\sqrt{2}a_{Cu_2O} = 6.106$ Å. Ozawa *et al.*[21] propose that Cu_2O(111) planes fit epitaxially with a (2×2) supercell of ZnO(0001) with a lattice mismatch of −7% (i.e., the Cu_2O overlayer is subjected to tensile stress). In this orientation, the $[\bar{1}10]$ direction of Cu_2O runs parallel to the ZnO $[1\bar{2}10]$ direction. We also consider here an alternative fit in which the Cu_2O(111) overlayer is rotated by 30° in order to be matched with a $(\sqrt{3} \times \sqrt{3})$R30° supercell of ZnO(0001). In this case,

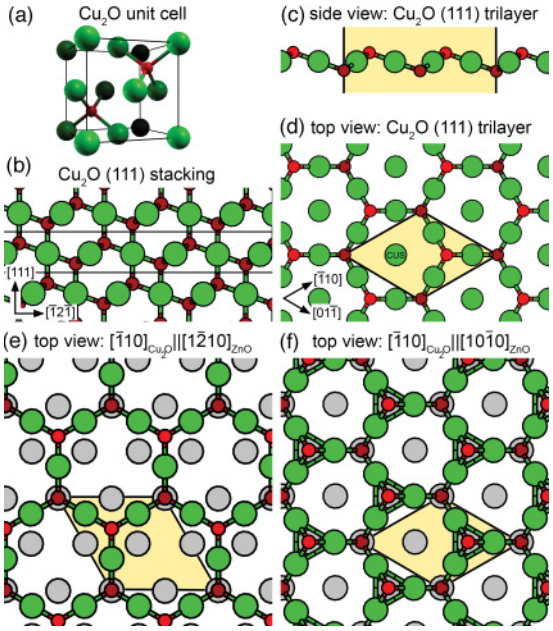

FIG. 19. (Color online) (a) Perspective view of the cubic unit cell of Cu_2O. (b) Side view of Cu_2O with the [111] axis in the vertical direction. This view illustrates the vertical stacking of Cu_2O(111) trilayers. An isolated trilayer is shown in side and top views in panels (c) and (d) with the hexagonal unit cell indicated by background shading. Panels (e) and (f) show, respectively, how a single Cu_2O(111) trilayer can be matched with a (2×2) and $(\sqrt{3} \times \sqrt{3})$R30° supercell of ZnO(0001).

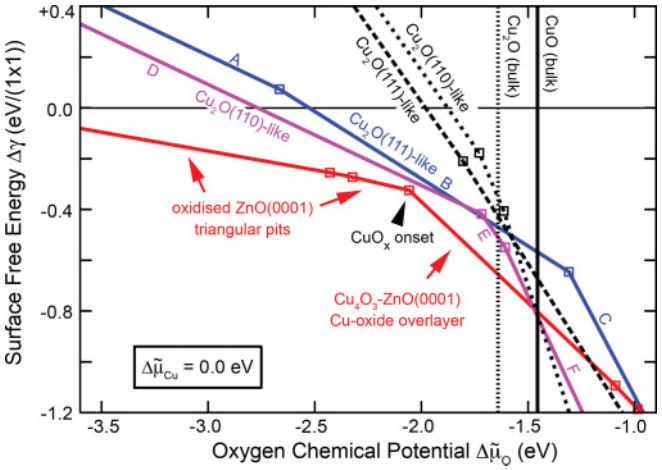

FIG. 20. (Color online) Phase stability diagram comparing the Cu_2O-like overlayer structures with the minimum free-energy curve (solid, red lines) of the stable oxidized ZnO(0001) (triangular pit) phases as well as the Cu_4O_3-ZnO(0001) phase. Shown are four additional free-energy curves for $Cu_2O(111)$-like and $Cu_2O(110)$-like structures as overlayers on bulk-like ZnO(0001) (solid lines) and Cu_4O_3-ZnO(0001) (dashed lines). Vertical solid and dotted lines indicate the phase boundaries to bulk CuO and Cu_2O precipitation.

$[\bar{1}10]_{Cu_2O}\|[10\bar{1}0]_{ZnO}$ and the lattice mismatch is +7%; that is, the overlayer experiences compressive stress.

In order to test the stability of such overlayer structures, we have placed a single $Cu_2O(111)$ trilayer onto bulklike ZnO(0001) (2×2) and $(\sqrt{3} \times \sqrt{3})R30^\circ$ with various in-plane registries. The preferred registries for the two supercells are shown in Figs. 19(e) and 19(f); in both cases, the atoms of the lower oxygen plane are positioned in top configuration relative to the Zn atoms of the substrate and the Cu_{CUS} atom is absent. The inclusion of the Cu_{CUS} atoms led to much higher free energies. To these single-trilayer overlayer structures we then added up to two more trilayers to create structures with a thicker $Cu_2O(111)$ overlayer. Only in the case of a triple-trilayer structure is there a Cu_{CUS} atom present in the center trilayer.

The phase stability diagram in Fig. 20 examines the free energies of this set of "$Cu_2O(111)$-like" structures. The diagram is plotted with respect to the oxygen chemical potential, $\Delta\tilde{\mu}_O$ with the copper chemical potential set to 0.0 eV; that is, we analyze the phase stability along the boundary to bulk-Cu precipitation. Other applicable bulk constraints at $\Delta\tilde{\mu}_{Cu} = 0$ eV are indicated using vertical lines: The bulk oxides Cu_2O and CuO are expected to form at an oxygen chemical potential of −1.64 eV (dotted line) and −1.46 eV (solid line), respectively. For brevity, we show only the minimum free-energy curve for each set of structures. The lowest (red) minimum free-energy curve in Fig. 20 is referred to in the following as the "reference curve." This curve represents the globally favored structures in this chemical potential regime, namely, the triangular pit phases of the Cu-free surface at $\Delta\tilde{\mu}_O < -2.07$ eV, transitioning into the $(\sqrt{3} \times \sqrt{3})R30^\circ$ Cu_4O_3-ZnO(0001) and $Cu_{12}O_{13}$-ZnO(0001) copper-oxide overlayer phases (above $\Delta\tilde{\mu}_O = -2.07$ and −0.99 eV, respectively). Of particular interest here is the vicinity of the transition point (black arrowhead in Fig. 20), marking the onset of Cu-oxide overlayer formation. This is the phase region in which the Cu_2O-like structures are most likely to appear as a minimum free-energy phase.

The (blue) free-energy curve in Fig. 20 labeled "$Cu_2O(111)$-like" represents the three favored phases of the set of $Cu_2O(111)$ overlayer structures discussed above. In order from low to high $\Delta\tilde{\mu}_O$, these are the single-trilayer phase on (2×2) ZnO(0001) [labeled "A" in Fig. 20; structure in Fig. 19(d)], the single-trilayer phase on $(\sqrt{3} \times \sqrt{3})R30^\circ$ ZnO(0001) ["B" and Fig. 19(e)], and a triple-trilayer structure on $(\sqrt{3} \times \sqrt{3})R30^\circ$ ZnO(0001) ("C"). Against these three phases, a double-trilayer phase was not stable, and thus the free-energy curve transitions directly from a single- to a triple-trilayer phase. Overall, we can see that the $Cu_2O(111)$-like free-energy curve is less stable than the reference curve for most of the $\Delta\tilde{\mu}_O$ range shown. Only at $\Delta\tilde{\mu}_O = -0.93f$ eV, that is, well into the regime of bulk CuO precipitation, does a crossing with the reference curve occur. Closest in free energy to the reference curve outside of a bulk-precipitation regime is the single $Cu_2O(111)$ trilayer $(\sqrt{3} \times \sqrt{3})R30^\circ$ phase with a free-energy slope that is intermediate between the stable triangular pit and the Cu_4O_3-ZnO(0001) phases. However, the stability of this $Cu_2O(111)$ phase is insufficient to intersect the reference curve and become a stable phase itself.

We have similarly placed $Cu_2O(111)$ trilayers as overlayers onto the Cu_4O_3-ZnO(0001) phase. This was done to ascertain whether the Cu_4O_3 overlayer would offer a more favorable linkage to any $Cu_2O(111)$ overgrowth. As before, the $Cu_2O(111)$ trilayers were lattice matched with (2×2) and $(\sqrt{3} \times \sqrt{3})R30^\circ$ supercells of the substrate, and, again, the preferred in-plane registry is the one that positions the lower oxygen atoms of the trilayer at the top site relative to the Cu atoms of the substrate surface. The resultant minimum free-energy curve of the structures in this set is also labeled "$Cu_2O(111)$-like" in Fig. 20 and plotted using dashed lines. Over the relevant $\Delta\tilde{\mu}_O$ range shown, only the single-trilayer phases contribute to this curve, namely, the (2×2) phase and $(\sqrt{3} \times \sqrt{3})R30^\circ$ phase at lower and higher $\Delta\tilde{\mu}_O$, respectively. The $(\sqrt{3} \times \sqrt{3})R30^\circ$ phase crosses the (red) reference curve at high $\Delta\tilde{\mu}_O$; however, this again occurs only within the regime of bulk CuO precipitation.

$Cu_2O(110)$-like overlayers. We also explored possible overlayer structures that result when Cu_2O is placed with its (110) face onto ZnO(0001). Such an orientation was found in recent chemical vapor deposition experiments[66] in which thin films of Cu_2O are grown on ZnO. The in-plane unit cell of $Cu_2O(110)$ is rectangular, as shown in Fig. 21(a), with calculated lattice constants of 6.106 and 4.317 Å along $[\bar{1}10]$ and [001], respectively. In the plane-perpendicular, [110] direction, Cu_2O is described by an alternate stacking of two types of atomic planes, namely, a plane of "zigzag" –O–Cu–O–Cu–O– chains of nominal CuO stoichiometry and a rectangular plane containing only Cu atoms.

The rectangular unit cell of $Cu_2O(110)$ may conceivably fit with a rectangular $(2 \times \sqrt{3}R30^\circ)$ supercell of the ZnO(0001) with lattice constants of 6.579 and 5.697 Å [see Fig. 21(b)]. The resultant mismatch of −7% and −24%, respectively, suggests a passable fit in one direction, namely, $[\bar{1}10]_{Cu_2O}\|[1\bar{2}10]_{ZnO}$, and considerable tensile stress in the

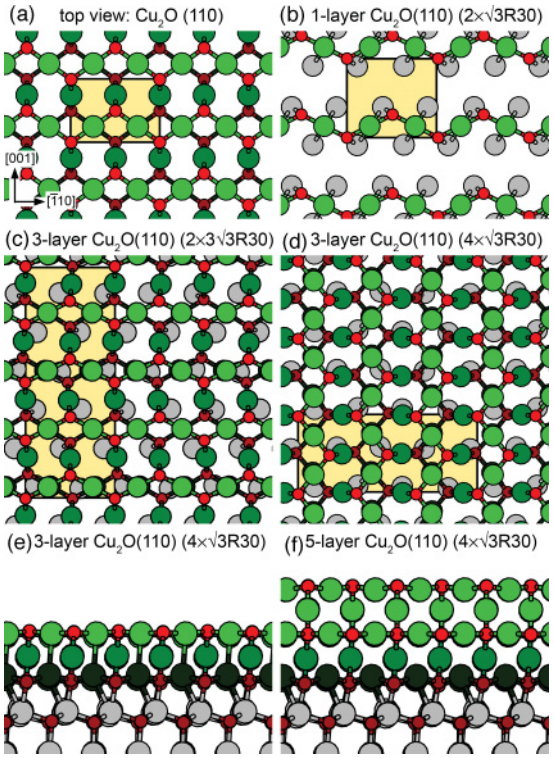

FIG. 21. (Color online) $Cu_2O(110)$-like structures on ZnO(0001). Panel (a) shows a view of bulk Cu_2O along the [110] direction. The rectangular unit cell of $Cu_2O(110)$ is indicated by background shading. In panel (b) the O–Cu–O–Cu– zigzag atomic plane of $Cu_2O(110)$ is matched with a $(2 \times \sqrt{3}R30^\circ)$ supercell of ZnO(0001). (c),(d) Thicker, three-layer slabs of $Cu_2O(110)$ are more favorably matched with $(2 \times 3\sqrt{3}R30^\circ)$ and $(4 \times \sqrt{3}R30^\circ)$ supercells of ZnO(0001). (e),(f) Side views of three-layer and five-layer $Cu_2O(110)$ phases, respectively, on $(4 \times \sqrt{3}R30^\circ)$ ZnO(0001).

other direction ($[001]_{Cu_2O} \| [10\bar{1}0]_{ZnO}$). Fitting a larger $(2 \times 3\sqrt{3}R30^\circ)$ supercell of ZnO(0001) with a (1×4) supercell of $Cu_2O(110)$ [see Fig. 21(c)] reduces the mismatch along $[001]_{Cu_2O}$ to a mere $+1\%$, promising a much more effective lattice match. An alternative fit has been proposed in Ref. 66 and it is achieved by rotating a (3×1) supercell of $Cu_2O(110)$ by 90° and fitting it with a $(4 \times \sqrt{3}R30^\circ)$ supercell of ZnO(0001) as shown in Fig. 21(d). In this combination, $[001]_{Cu_2O} \| [1\bar{2}10]_{ZnO}$ (and $[\bar{1}10]_{Cu_2O} \| [10\bar{1}0]_{ZnO}$), producing a lattice mismatch of -2 and $+7\%$, respectively. In the following, we refer to these three types of lattice matchings simply in terms of the substrate supercell as the $(2 \times \sqrt{3}R30^\circ)$, the $(2 \times 3\sqrt{3}R30^\circ)$, and the $(4 \times \sqrt{3}R30^\circ)$ sets of $Cu_2O(110)$-like structures.

Within each of these sets, various structures were generated by stacking up to five $Cu_2O(110)$ atomic planes onto ZnO(0001), alternating between the CuO-stoichiometric zigzag planes and the rectangular Cu plane. Only three of these structures contribute to the minimum free-energy curve for this set, plotted in solid (purple) lines in Fig. 20 and labeled "$Cu_2O(110)$-like." From low to high $\Delta\tilde{\mu}_O$ these structures are a single O–Cu–O–Cu–O zigzag atomic plane from the $(2 \times \sqrt{3}R30^\circ)$ set (labeled "D" in Fig. 20) as well as a three-layer structure and a five-layer structure from the $(4 \times \sqrt{3}R30^\circ)$ set (labeled "E" and "F", respectively).

The first of these structures,"D", is shown in Fig. 21(b) and is the one that comes closest of *all* the Cu_2O-like overlayer structures to intersecting with the reference curve outside the bulk constraints, and forming a stable surface phase. We believe this is primarily due to the fact that this phase is structurally closest to the stable Cu_4O_3-ZnO(0001) phase, and may be regarded as an incomplete precursor thereof. In order to demonstrate this, we have set up for geometry optimization a variant of the structure in Fig. 21 in which the zig-zag lines are moved closer to one another by one ZnO(0001) lattice vector, which, in effect, doubles the density of CuO zigzag chains. The relaxation of this trial structure produced the Cu_4O_3-ZnO(0001) phase. The other two structures contributing to the $Cu_2O(110)$ phase curve, "E" and "F", are shown in Figs. 21(d) to 21(f) and can be considered as thin slabs of $Cu_2O(110)$ on ZnO(0001), with both presenting a Cu-O zigzag atomic plane at the interface with the ZnO(0001) surface and the vacuum. Earlier results[51] have shown that the (110) surface of bulk Cu_2O terminates at a Cu-O zigzag atomic plane. In this regard, these two thin-slab structures already behave like bulk Cu_2O. It is also interesting to note that in these overlayer structures, the $(1 \times 3)_{Cu_2O(110)}$:$(4 \times \sqrt{3}R30^\circ)_{ZnO(0001)}$ lattice match wins out in stability over the alternative $(1 \times 4)_{Cu_2O(110)}$:$(2 \times 3\sqrt{3}R30^\circ)_{ZnO(0001)}$ match, which does not contribute to the $Cu_2O(110)$-like phase curve.

As was done for the $Cu_2O(111)$-like phases, we also generated $Cu_2O(110)$-like structures on top of a Cu_4O_3-ZnO(0001) substrate. The resultant phase curve is shown using dotted lines in Fig. 20 and labeled "$Cu_2O(110)$-like." Three structures contribute to this phase curve and they are the direct Cu_4O_3-ZnO(0001) analogs to the three contributing phases on a bulklike ZnO(0001) substrate, namely, a single Cu-O zigzag plane on a $(2 \times \sqrt{3}R30^\circ)$ supercell of Cu_4O_3-ZnO(0001), as well as a three-layer and a five-layer $Cu_2O(110)$ overlayer in a $(4 \times \sqrt{3}R30^\circ)$ supercell. As the phase diagram shows, these phases are the least stable of the Cu_2O-like structures in the allowed range of the oxygen chemical potential; only within the bulk constraints does the $Cu_2O(110)$-like phase stability curve cross the reference curve.

Summarizing our results for the Cu_2O-like structures, we find that *none* of the considered structures is thermodynamically viable as a stable overlayer phase.

IV. DISCUSSION

The primary result of our extensive computational survey of the Cu/ZnO(0001) system is a two-dimensional phase diagram (Fig. 2) that identifies the stable surface structures as a function of the oxygen and copper chemical potentials. We have replotted this diagram in Fig. 22 with every stable phase labeled, and the horizontal $\Delta\tilde{\mu}_O$ axis translated into oxygen partial pressures for two temperatures regimes (650 K and 1000 K). This diagram provides the theoretical framework that we now use to discuss the relevant experimental literature.

The phase diagram posits the existence of three stable copper-oxide monolayer structures that are thermodynamically stable within a reasonably wide window (red shaded in Fig. 22) between the Cu-free ZnO(0001) surface and

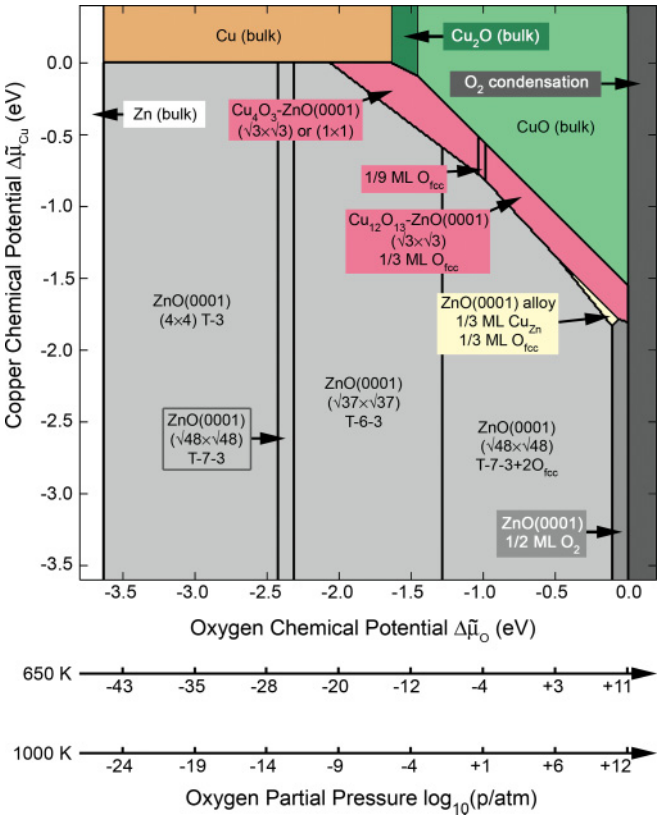

FIG. 22. (Color online) Two-dimensional phase diagram showing the principal surface structure regimes of the Cu/ZnO(0001) system as a function of the copper and oxygen chemical potential.

bulk copper/copper-oxide. The two most prominent phases in this regime are the Cu_3O_4-ZnO(0001) phase at more reducing conditions, and a $Cu_{12}O_{13}$-ZnO(0001) phase under more oxygen-rich conditions. Both phases are structurally characterized by $(\sqrt{3} \times \sqrt{3})$R30° unit cell; however, we note that the Cu_3O_4-ZnO(0001) phase can present under certain circumstances as a (1×1) phase due to thermal averaging over degenerate configurations (as detailed in Sec. III E). Under highly reducing conditions ($\Delta\tilde{\mu}_O < -2.1$ eV), Cu-containing surface structures are not stable in our phase diagram. Instead, there is a direct transition at $\Delta\tilde{\mu}_{Cu} = 0$ eV from a Cu-free ZnO(0001) surface to a regime were bulk Cu is expected to form.

It is important to remember that these predictions assume that full thermodynamic equilibrium has been established between the participating bulk, surface, and gas phases. In experimental practice this assumption will not always apply, in which case the phase diagram can only provide guidance as to the general direction that the system will evolve toward. In such a state of nonequilibrium, temperature takes on a dual role influencing both the point of thermodynamic equilibrium (e.g., through the oxygen chemical potential) as well as the kinetic rate with which the system progresses toward this equilibrium (see, e.g., Ref. 67). With this in mind, we now discuss, in turn, the observation of Cu(111) nanoparticles on the ZnO(0001) surface, and the experimental evidence for the copper oxide monolayer phases proposed herein.

Copper nanoparticle formation on ZnO(0001). A number of experimental studies[14,15,17–19,21] describe the deposition of metallic Cu on the (0001) face of single crystal ZnO samples. Yoshihara *et al.*[14,15] describe a coverage-dependent transition between a two-dimensional (i.e., monolayer) and three-dimensional growth mechanism for Cu on ZnO(0001). Direct imaging of Cu nanoparticle growth using scanning tunneling microscopy was reported by Koplitz *et al.*[17], Dulub *et al.*,[18] and Kroll and Köhler.[19] These latter sets of experiments in particular illuminate the role of surface defects and surface roughness as precipitation sites for Cu particle growth. Measurements of the imaged Cu deposits find both monolayer and multiple-layer thicknesses at all coverages. These authors also show that heating facilitates the transition from two-dimensional to three-dimensional growth.[17–19] This role of temperature strongly points to some form of kinetic limitation in these deposition experiments.

How are these observations compatible with our phase diagram which stipulates a direct transition from Cu-free ZnO(0001) to bulk Cu? An important technical detail to consider here is that any bulk copper formed in the course of a real deposition experiment will not be entirely composed of "pure" bulk from an energetics perspective. Any precipitate will invariably expose some form of a surface which influences the energetics in detail. These precipitate surface effects are not captured by the thermodynamical constraints that define the bulk boundaries in Fig. 22. As applied, the constraints inform us only on the conditions when bulk precipitates are formed; however, the constraints do not resolve whether these bulk particles will form an interface with ZnO(0001).

A full characterization of the interface between bulk Cu and ZnO(0001) is beyond the scope of this work; however, we can fairly simply assess whether bulk Cu forms a stable interface with two specific ZnO(0001) surface phases, namely, bulklike ZnO(0001) and Cu_3O_4-ZnO(0001). Table IX reports the calculated interfacial energy, ϵ, for thin, n-layer slabs of Cu(111) in vacuum and adsorbed on these two substrate surfaces. The interfacial energy for the n-layer slab in vacuum is calculated as

$$\epsilon = \frac{1}{A}(E_{Cu(111)} - N_{Cu}E_{Cu}), \tag{21}$$

where $E_{Cu(111)}$ and E_{Cu} are the calculated energy of the Cu (111) slab and an atom of bulk Cu, respectively. N_{Cu} is the number of Cu atoms in the slab and A is the total surface area of the slab (counting two sides). We see in Table IX that the interfacial energy converges to a value of approximately 0.48 eV per (1×1) unit cell (or 1.3 J/m^2) with increasing slab thickness n. This value corresponds to the surface energy of Cu(111) and is in good agreement with the results of earlier calculations (0.52 and 0.50 eV in Refs. 50 and 68, respectively) and is a small underestimate of the experimental value (1.8 J/m^2; Ref. 69) as is typical for DFT calculations in the GGA.

It is instructive to recast this surface energy into an effective cohesive energy for a Cu atom at the surface, assuming that the energy for all other atoms is equal to that of bulk copper. This surface cohesive energy[62] is simply calculated as the surface energy per surface atom plus the bulk cohesive energy (−3.49 eV), giving a value of −3.01 eV. This type of analysis

highlights the following: While *all* Cu adatom/overlayer structures considered in Secs. III C and III D have adsorption energies that are *less* stable than Cu atoms in bulk, some of these structures are *more* favorable than the Cu atoms at the Cu(111) surface. This suggests that there should be strong adhesion between bulk Cu(111) and ZnO(0001).

Our direct adhesion calculations between an n-layer Cu(111) slab and the two substrate surfaces—bulklike ZnO(0001) and Cu_4O_3-ZnO(0001)—bear this out. Reaction energies of adhesion, $\Delta\epsilon$, are computed using the expression

$$\Delta\epsilon = \frac{1}{A}(E_{\text{sub+Cu(111)}} - E_{\text{sub}} - E_{\text{Cu(111)}} - N_{\text{Cu}}\delta E_{\text{strain}}), \tag{22}$$

where, in addition to the energy terms used in Eq. (21), $E_{\text{sub+Cu(111)}}$ represents the energy of the substrate in contact with the Cu(111) slab. The surface area A in this case is the interfacial area between the two materials. The last term in the equation represents a strain correction that accounts for the residual lattice mismatch when Cu(111) is placed on ZnO(0001) within the artificial confines of a common periodic unit cell. In our calculations we use the (4×4):(3×3) supercell combination discussed in Sec. III C with a residual mismatch of $+5\%$, causing the in-plane repeat of the Cu(111) slab to be slightly compressed. The energy per Cu atom associated with this compression is denoted δE_{strain} in Eq. (22), which we approximate *ad hoc* using a Cu(111) slab compressed by an equivalent amount in vacuum.

The data in Table IX show that the Cu(111) adhesion energy is negative (i.e., thermodynamically favorable) for both the bulklike ZnO(0001) surface and the Cu_4O_3-ZnO(0001) phase, converging with Cu(111) slab thickness, n, to values of approximately -0.6 and -0.3 eV/(1×1), respectively (or -1.7 and -0.8 J/m^2). These values are somewhat smaller in magnitude than the experimental estimations of -3.00 ± 0.10 J/m^2 (Refs. 9 and 62) and -3.4 ± 0.1 J/m^2 (Ref. 17) via the Wulff equilibrium geometry of deposited copper particles. Of the two substrates considered by us, the adhesion energy between the bulklike ZnO(0001) surface and Cu(111) is closer to the experimental value, suggesting that this is the better representation of the experimental interface. However, other interface geometries could conceivably lead to more stable adhesion and neither is it entirely clear to what particular ZnO surface structure the Cu particles are bonded to in experiment. In this respect, our calculated energies of adhesion may be considered an upper bound and reasonably consistent with experiment. We can rationalize the observation of Cu deposition on ZnO(0001) as the experimental manifestation of the copper chemical potential reaching the $\Delta\tilde{\mu}_{\text{Cu}} = 0$ eV boundary in our phase diagram (Fig. 22). In line with the arguments of Refs. 9 and 17, copper particles appear on the surface and they are bonded to the ZnO substrate because the Cu(111):ZnO(0001) interface is more stable than the two faces exposed to vacuum.

TABLE IX. The calculated surface energy, ϵ [in eV per Cu(111) (1×1)], for an n-layer Cu(111) slab in vacuum and the adhesion energy, $\Delta\epsilon$ (same unit), of interfacing the slab with the bulklike ZnO(0001) and Cu_4O_3-ZnO(0001) surface. Also reported for Cu(111) in vacuum is the strain energy δE_{strain} (in meV per Cu atom) due to residual lattice mismatch to fit a (4×4) supercell of Cu(111) with a (3×3) supercell of the ZnO(0001) substrate.

	Vacuum		ZnO(0001)	Cu_4O_3-ZnO(0001)
n	ϵ	δE_{strain}	$\Delta\epsilon$	$\Delta\epsilon$
1	+0.40	−80	−0.54	−0.21
2	+0.47	−14	−0.58	−0.25
3	+0.50	+6	−0.63	−0.29
4	+0.49	+18	−0.60	−0.25
5	+0.49	+26	−0.61	−0.29
10	+0.48	+37	—	—

In the thermodynamic ideal, these Cu particles would seek to minimize their surface free energy and maximize the number of Cu atoms that are bulklike. This in turn should drive Cu atoms to agglomerate into fewer and larger particles, provided the relevant kinetic barriers can be overcome. In the experiments described by Dulub *et al.*[18] and Koplitz *et al.*,[17] such an agglomeration of Cu particles appears to be suppressed at room temperature and is still incomplete following a 650 K anneal. Kroll and Köhler[19] using *in situ* STM imaging experiments were able to observe some "undercritical" clusters to decay even at room temperature and other clusters to grow. These reactions are clearly steps toward more bulklike Cu on the surface, in line with our finding of higher thermodynamic stability with increasing Cu(111) thickness, yet full agglomeration appears to remain kinetically suppressed. Under the prevailing conditions in these experiments, the ZnO(0001) surface effectively acts as a surfactant, stabilizing the surface energy of Cu(111), which helps to disperse metallic Cu over the surface into nanoparticles. This surfactant, nanodispersive role of the ZnO surface on Cu could be an important contributing factor toward the high efficiency of the Cu/ZnO catalytic system.

Copper oxide monolayers on ZnO(0001). Under more oxygen-rich condition, our phase diagram (Fig. 22) identifies a distinct regime of copper oxide monolayer phases with $(\sqrt{3} \times \sqrt{3})$R30° unit cells. Compelling experimental evidence for the latter phase is provided by the LEED experiments of Dulub *et al.*,[18] reporting a $(\sqrt{3} \times \sqrt{3})$R30° superstructure when Cu particles deposited on ZnO(0001) are annealed to 650 K in an oxygen-containing environment ($p_{O_2} = 10^{-9}$ atm). It is also shown[18] that a change of the annealing conditions to 900 K in vacuum ($p_{\text{chamber}} < 10^{-13}$ atm) and the aforementioned oxygen environment at 650 K result, respectively, in a reversible disappearance and reappearance of this superstructure.

These experimental findings are very consistent with our copper-oxide overlayer phases. The reported oxygen environment ($p_{O_2} = 10^{-9}$ atm, $T = 650$ K) giving rise to the $(\sqrt{3} \times \sqrt{3})$R30° pattern corresponds to an approximate oxygen chemical potential of $\Delta\tilde{\mu}_{\text{O}} = -1.3$ eV. This value is clearly within the oxygen potential range (-2.1 to -1.0 eV) where our Cu_4O_3-ZnO(0001) phase is stable, provided that $\Delta\tilde{\mu}_{\text{Cu}}$ is sufficiently large. The conditions that lead to a disappearance of the superstructure pattern ($p_{O_2} < 10^{-13}$ atm and $T = 900$ K) result in a much lower oxygen chemical potential of $\Delta\tilde{\mu}_{\text{O}} < -2.2$ eV, which is just

outside of the boundary where the Cu_4O_3-ZnO(0001) phase is stable. The appearance/disappearance of the $(\sqrt{3}\times\sqrt{3})$R30° pattern is thus neatly explained as a crossing of the boundary at $\Delta\tilde{\mu}_O = -2.1$ eV between a Cu-free ZnO(0001) surface and the Cu_4O_3-ZnO(0001) overlayer phase in accordance with the applied annealing conditions (p_{O_2} and T).

Dulub *et al.*[18] proposed two structure models for their observed $(\sqrt{3}\times\sqrt{3})$R30° pattern, namely, a 1/3-ML alloy phase and an overlayer phase labeled as "Cu_3O_2." This latter phase is described [see Fig. 12(b) in Ref. 18] by a stacking sequence $O^C_{2/3}Cu^BZn^AO^B\cdots$, which means (cf. Sec. II E) the overlayer stoichiometry is more correctly described as $Cu_{12}O_5$ (i.e., an oxygen deficient Cu_2O). Both structure proposals, and site variants thereof, are included in our structure survey; however, neither was a minimum free-energy structure anywhere in the phase diagram.[70] In contrast, our Cu_4O_3-ZnO(0001) structure appears as a stable phase in Fig. 22 and is thus a highly plausible candidate for the observed $(\sqrt{3}\times\sqrt{3})$R30° LEED pattern.

X-ray photoelectron spectroscopy and LEED experiments reported by Ozawa *et al.*[21] provide additional evidence that a copper oxide overlayer is formed when deposited copper on ZnO(0001) is exposed to oxygen at 650 K. With very similar conditions as used by Dulub *et al.*,[18] the authors were able to produce overlayers with a (1×1) LEED pattern, but did not observe the $(\sqrt{3}\times\sqrt{3})$R30° phase. On the basis of the recorded Cu-2p XPS shifts, they attribute the overlayer stoichiometry to be Cu_2O. The proposed (111) orientation of the Cu_2O overlayer is primarily motivated[21,71] by the favorable lattice mismatch of −7%. Ozawa *et al.* describe how the Cu_2O(111) atomic planes could plausibly fit onto ZnO(0001). Based on our results, we believe this structure model is problematic on three grounds. First, lattice mismatch arguments alone are insufficient to justify a Cu_2O(111) orientation as other orientations, including Cu_2O(110), may equally "fit." Second, none of the Cu_2O-like overlayer structures considered by us in Sec. III I is thermodynamically stable in our phase diagram; in all cases, the Cu_4O_3-ZnO(0001) phase is the more stable Cu-oxide overlayer phase, which strongly suggests that this is the phase formed in the Ozawa *et al.*[21] experiments. Third, and as already acknowledged in Ref. 21, a Cu_2O(111)-like overlayer should lead to a superstructure in their LEED experiments, either a (2×2) or a $(\sqrt{3}\times\sqrt{3})$R30° superstructure [cf. Figs. 19(c) and 19(d)]; however, only a (1×1) pattern is found. In contrast, the Cu_4O_3-ZnO(0001) phase is consistent with a (1×1) pattern, provided that dynamic averaging over degenerate $(\sqrt{3}\times\sqrt{3})$R30° configurations occurs. The difference in the observed LEED patterns between the Dulub *et al.*[18] and Ozawa *et al.*[21] experiments—$(\sqrt{3}\times\sqrt{3})$R30° in the former, (1×1) in the latter—may thus be attributed to differences in the effect of, for example, phase boundaries and step edges to suppress the averaging process.

There is also the possibility that Ozawa *et al.*[21] have formed a thicker, more bulklike Cu_2O overlayer with an epitaxial fit between ZnO(0001) and bulk Cu_2O, similar to Cu_2O:ZnO interfaces produced by Jeong *et al.*[66] using chemical vapor deposition techniques. Such bulk-Cu_2O structures on ZnO(0001) would correspond to the regime of bulk-Cu_2O precipitation in our phase diagram (Fig. 22), provided there is an exothermic adhesion energy between ZnO(0001) and the surfaces of any bulk Cu_2O particles formed. For the Cu_2O(110) surface, our *ad hoc* evaluation in Table X suggest that this is the case. The calculated adhesion energy of placing three- and five-layer slabs of Cu_2O(110) onto a bulklike ZnO(0001) is sharply negative for both a $(1\times3)_{Cu_2O(110)}$:$(4\times\sqrt{3}$R30°$)_{ZnO(0001)}$ and a $(1\times4)_{Cu_2O(110)}$:$(2\times3\sqrt{3}$R30°$)_{ZnO(0001)}$ lattice match. This is to say, it is preferable for an exposed Cu_2O(110) surface and a bulklike ZnO(0001) surface to interface with one another, instead of being separately exposed to vacuum. The calculated adhesion energy of Cu_2O(110) with the Cu_4O_3-ZnO(0001) surface is considerably smaller.

TABLE X. The calculated adhesion energy, $\Delta\epsilon$ [in eV per Cu_2O(110) (1×1) surface unit], of three- and five-layer Cu_2O(110) slabs on bulklike ZnO(0001) and Cu_4O_3-ZnO(0001). Adhesion energies are reported for two lattice orientations as defined by the substrate supercell used (see text), namely, $(4\times\sqrt{3}$R30°$)$ and $(2\times3\sqrt{3}$R30°$)$, which are matched with (3×1) and (4×1) supercells of Cu_2O(110), respectively.

Slab	Supercell	ZnO(0001) $\Delta\epsilon$	Cu_4O_3-ZnO(0001) $\Delta\epsilon$
Three-layer	$(4\times\sqrt{3}$R30°$)$	−2.79	−0.62
	$(2\times3\sqrt{3}$R30°$)$	−2.44	−0.28
Five-layer	$(4\times\sqrt{3}$R30°$)$	−2.66	−0.50
	$(2\times3\sqrt{3}$R30°$)$	−2.36	−0.21

Further evidence for the existence of a copper oxide monolayer phase is provided by the STM experiments of Kroll and Köhler.[19] Their annealing experiments find that the substrate surface surrounding a Cu particle undergoes a characteristic change at annealing temperatures of 470 K (and higher), which is described as "entrenching." We believe these observations are consistent with the formation of a copper oxide monolayer phase in the vicinity of a Cu particle which could be either the $Cu_{12}O_{13}$-ZnO(0001) or the Cu_4O_3-ZnO(0001) phase, depending on the prevailing oxygen chemical potential conditions. The reported 470 K annealing temperature is presumably the minimum required to activate the transformation of bulk Cu into a copper oxide overlayer phase. Utilizing oxygen adatoms from the substrate surface, and the odd, residual oxygen atom taken up from vacuum, the copper oxide overlayer is likely to form as an *adlayer* near the Cu particle, thus giving the appearance of the particle to sink into the substrate, or "entrench" in the words of Ref. 19. The reported chamber base pressure of 6×10^{-14} atm provides an upper bound for the oxygen partial pressure which we combine with the annealing temperature to an estimated oxygen chemical potential of $\Delta\tilde{\mu}_O = -1.1$ eV. As seen in Fig. 22, these conditions are well within the regime of the copper-oxide overlayer phases, even if we allow for p_{O_2} to be several orders of magnitude below the chamber base pressure. For surfaces annealed to 670 K, Kroll and Köhler[19] report that the triangular reconstruction of the ZnO substrate has disappeared, which is also in line with our phase diagram and a transition from the regime of triangular pits (gray shading in Fig. 22) to the flat copper oxide overlayer phases (red shading).

V. SUMMARY

Using DFT calculations combined with the *ab initio* atomistic thermodynamics approach, we have constructed a two-dimensional phase diagram for the ZnO(0001) surface in a copper and oxygen environment. Our calculations identify distinct copper oxide overlayer phases with $(\sqrt{3} \times \sqrt{3})$R30° unit cells, which are thermodynamically stable in a chemical potential window between the Cu-free ZnO(0001) reconstructions and bulk Cu/Cu-oxide precipitation. These overlayer phases are consistent with experiments[18] reporting for mildly oxidizing conditions a stable Cu overlayer phase on ZnO(0001) with a $(\sqrt{3} \times \sqrt{3})$R30° LEED pattern. Our calculations provide with the Cu_4O_3-ZnO(0001) structure shown in Figs. 14(a) and 14(b) a highly plausible assignment for this experimental phase. Under more reducing conditions, we find that Cu does not bind to the ZnO(0001) surface; our phase diagram suggests a sharp transition between the Cu-free ZnO(0001) surface phase and the precipitation of bulk Cu particles. Experimental observations of copper deposition are consistent with our phase diagram, keeping in mind that bulk-Cu forms a stable interface with ZnO(0001) via its (111) crystal phase. It is noted, though, that most Cu deposition experiments are conducted in a kinetically limited regime, and full agreement with a thermodynamic phase diagram should not be expected.

ACKNOWLEDGMENTS

This work was supported by the Australian Research Council under Discovery Grant No. DP0770631. Computational resources are provided by the Australian National Computational Infrastructure (NCI).

*o.warschkow@physics.usyd.edu.au

[1] M. S. Spencer, Top. Catal. **8**, 259 (1999).
[2] T. Fujitani and J. Nakamura, Appl. Catal., A **191**, 111 (2000).
[3] H. Purnama, T. Ressler, R. E. Jentoft, H. Soerijanto, R. Schlögl, and R. Schomäcker, Appl. Catal., A **259**, 83 (2004).
[4] G. W. Bridger and M. S. Spencer, *Catalyst Handbook*, 2nd ed., edited by M. V. Twigg (Wolfe Publishing, London, 1989).
[5] S. I. Fujita, M. Usui, and N. Takezawa, J. Catal. **134**, 220 (1992).
[6] E. I. Solomon, P. M. Jones, and J. A. May, Chem. Rev. **93**, 2623 (1993).
[7] J. B. Hansen and P. E. H. Nielsen in *Handbook of Heterogeneous Catalysis*, edited by G. Ertl, H. Knötzinger, and J. Weitkamp (VCH, Weinheim, 2008).
[8] J. Nakamura, Y. Choi, and T. Fujitani, Top. Catal. **22**, 277 (2003).
[9] P. L. Hansen, J. B. Wagner, S. Helveg, J. R. Rostrup-Nielsen, B. J. Clausen, and H. Topsøe, Science **295**, 2053 (2002).
[10] J. B. Wagner, P. L. Hansen, A. M. Molenbroek, H. Topsoe, B. S. Clausen, and S. Helveg, J. Phys. Chem. B **107**, 7753 (2003).
[11] J. Yoshihara and C. T. Campbell, J. Catal. **161**, 776 (1996).
[12] S. V. Didziulis, K. D. Butcher, S. L. Cohen, and E. I. Solomon, J. Am. Chem. Soc. **111**, 7110 (1989).
[13] C. T. Campbell, Surf. Sci. Rep. **27**, 1 (1997).
[14] J. Yoshihara, J. M. Campbell, and C. T. Campbell, Surf. Sci. **406**, 235 (1998).
[15] J. Yoshihara, S. C. Parker, and C. T. Campbell, Surf. Sci. **439**, 153 (1999).
[16] P. J. Møller, S. A. Komolov, E. F. Lazneva, and T. Egebjerg, Appl. Surf. Sci. **142**, 210 (1999).
[17] L. V. Koplitz, O. Dulub, and U. Diebold, J. Phys. Chem. B **107**, 10583 (2003).
[18] O. Dulub, M. Batzill, and U. Diebold, Top. Catal. **36**, 65 (2005).
[19] M. Kroll and U. Köhler, Surf. Sci. **601**, 2182 (2007).
[20] P. Lazcano, M. Batzill, U. Diebold, and P. Häberle, Phys. Rev. B **77**, 035435 (2008).
[21] K. Ozawa, Y. Oba, and K. Edamoto, Surf. Sci. **603**, 2163 (2009).
[22] S. T. Bromley, S. A. French, A. A. Sokol, C. R. A. Catlow, and P. Sherwood, J. Phys. Chem. B **107**, 7045 (2003).
[23] S. A. French, A. A. Sokol, S. T. Bromley, C. R. A. Catlow, and P. Sherwood, Top. Catal. **24**, 161 (2003).
[24] C. R. A. Catlow, S. A. French, A. A. Sokol, M. Alfredsson, and S. T. Bromley, Faraday Discuss. **124**, 185 (2003).
[25] S. A. French, A. A. Sokol, C. R. A. Catlow, and P. Sherwood, J. Phys. Chem. C **112**, 7420 (2008).
[26] I. Hegemann, A. Schwaebe, and K. Fink, J. Comput. Chem. **29**, 2302 (2008).
[27] I. Schmitt, K. Fink, and V. Staemmler, Phys Chem Chem Phys **11**, 11196 (2009).
[28] B. Meyer and D. Marx, Phys. Rev. B **69**, 235420 (2004).
[29] X.-Q. Dai, H.-J. Yan, J.-L. Wang, Y.-M. Liu, Z. Yang, and M. H. Xie, J. Phys. Condens. Matter **20**, 095002 (2008).
[30] C. M. Weinert and M. Scheffler, Mater. Sci. Forum **10-12**, 25 (1986).
[31] M. Scheffler and J. Dabrowski, Philos. Mag. A **58**, 107 (1988).
[32] I. G. Batyrev, A. Alavi, and M. W. Finnis, Faraday Discuss. **114**, 33 (1999).
[33] I. G. Batyrev, A. Alavi, and M. W. Finnis, Phys. Rev. B **62**, 4698 (2000).
[34] K. Reuter and M. Scheffler, Phys. Rev. B **65**, 035406 (2001).
[35] K. Reuter and M. Scheffler, Phys. Rev. Lett. **90**, 046103 (2003).
[36] C. Stampfl, Catal. Today **105**, 17 (2005).
[37] B. Delley, J. Chem. Phys. **113**, 7756 (2000).
[38] J. P. Perdew, K. Burke, and M. Ernzerhof, Phys. Rev. Lett. **77**, 3865 (1996).
[39] B. Delley, Int. J. Quantum Chem. **69**, 423 (1998).
[40] To further illustrate this point, the spin polarization energy per unit area is less than 0.01 and 0.001 eV/(1 × 1) for, respectively, 83% and 74% of our set of surface structures.
[41] H. J. Monkhorst and J. D. Pack, Phys. Rev. B **13**, 5188 (1976).
[42] B. Meyer and D. Marx, Phys. Rev. B **67**, 035403 (2003).
[43] E. Kisi and M. M. Elcombe, Acta Crystallogr. Sect. C **45**, 1867 (1989).
[44] G. Kresse, O. Dulub, and U. Diebold, Phys. Rev. B **68**, 245409 (2003).
[45] A. Kokalj, Comput. Mater. Sci. **28**, 155 (2003).
[46] O. Dulub, U. Diebold, and G. Kresse, Phys. Rev. Lett. **90**, 016102 (2003).
[47] B. Meyer, Phys. Rev. B **69**, 045416 (2004).
[48] M. Valtiner, M. Todorova, G. Grundmeier, and J. Neugebauer, Phys. Rev. Lett. **103**, 065502 (2009).

[49]M. Valtiner, M. Todorova, and J. Neugebauer, Phys. Rev. B **82**, 165418 (2010).
[50]A. Soon, M. Todorova, B. Delley, and C. Stampfl, Phys. Rev. B **73**, 165424 (2006).
[51]A. Soon, M. Todorova, B. Delley, and C. Stampfl, Phys. Rev. B **75**, 125420 (2007); **76**, 129902(E) (2007).
[52]S. Piccinin, C. Stampfl, and M. Scheffler, Phys. Rev. B **77**, 075426 (2008).
[53]X. Duan, O. Warschkow, A. Soon, B. Delley, and C. Stampfl, Phys. Rev. B **81**, 075430 (2010).
[54]W. M. Haynes (editor), *CRC Handbook of Chemistry and Physics*, 91st ed. (CRC Press, Boca Raton, FL, 2010).
[55]Bulk copper oxide, CuO, is a strongly correlated, antiferromagnetic semiconductor that is poorly described by DFT in the GGA. The tenorite unit cell of CuO is monoclinic, while the DFT optimized unit cell is very nearly orthorhombic. Nevertheless, we find that the calculated transition chemical potential for CuO compares favorably with experiment (cf. Table II) when uniform chemical potential scaling is employed.
[56]M. J. Lyle, O. Warschkow, B. Delley, and C. Stampfl, Phys. Rev. B **82**, 165401 (2010).
[57]M. W. Finnis, Phys. Status Solidi A **166**, 397 (1998).
[58]O. Dulub, L. A. Boatner, and U. Diebold, Surf. Sci. **519**, 201 (2002).
[59]The addition of an oxygen adatom, O_{fcc}, to the ZnO(0001) surface consumes two electrons according to the nominal equation $\frac{1}{2}O_2 + 2e^- \rightarrow O^{2-}_{(ads.)}$ (see, e.g., Ref. 44). In the case of a positive oxygen excess, Γ_O (i.e., an oxygen coverage greater than 1/4 ML), these electrons are taken up from the valence band, resulting in the creation of electron holes. Formally, these holes may be assigned to the adatoms themselves, reducing their valency to a value smaller than −2. For example, in a (2 × 2) unit cell with a 1/2-ML coverage, the oxygen excess evaluates to 1/4 ML. This means that one of the two oxygen adatoms in the (2 × 2) unit is in excess, creating two holes. The distribution of these two holes over the two adatoms reduces the their formal valency from −2 to −1; that is, the adsorbed atoms may be regarded as O^- species.
[60]As defined in Ref. 44, a triangular pit of size n is composed of $n(n+1)/2$ zinc vacancies and $n(n-1)/2$ oxygen vacancies.
[61]An increase in the ZnO(0001) slab thickness leads to a small increase in the fcc Cu adsorption energies. For a coverage of 1-ML Cu, the adsorption energy changes from −2.642 eV for four ZnO double layers to −2.635 at six double layers and −2.615 eV at eight double layers. At 1/4-ML coverage, the calculated Cu adsorption energies are −2.478, −2.439, and −2.426 eV for four, six, and eight double layers, respectively. Increasing the vacuum gap from approximately 27 Å to 43 and 70 Å resulted in adsorption energy changes that were well below 1 meV.
[62]In this paper we attempt to conform for all energies (binding energies, surface energies, cohesive energies, adhesive energies, etc.) to the general sign convention that a more negative value corresponds to a more stable configuration. When citing the results of other works, we adjust the sign to be consistent with our use.
[63]The substitution of Zn atoms by Cu reduces the number of zinc atoms, N_{Zn}, in the slab which increases the oxygen excess Γ_O.
[64]We have confirmed that the calculated energy preference of approximately 20 meV per Cu_3 triangle is stable with respect to slab thickness, **k**-point density, and the electronic thermal broadening parameter. Increasing the slab size from four ZnO double layers to six and eight changes the calculated energy preference from 21 meV to 18 and 17 meV per Cu_3 triangle, respectively. A reduction of the thermal broadening parameter from 0.01 eV to zero reduced the energy preference by less than 2 meV. An increase of the **k**-point mesh from 10 × 10 to 16 × 16 and 22 × 22 changes the energy preference from 21 meV to 18 and 20 meV, respectively.
[65]In a nonpolarized DFT calculation (i.e., with spin-polarization suppressed), the relative stability reverses, with the high-symmetry (1 × 1) preferred by 0.05 eV per Cu_3 triangle over the low-symmetry $(\sqrt{3} \times \sqrt{3})$R30° phase. We note that the latter phase is still a minimum on the non-polarized potential energy surface.
[66]S.-H. Jeong and E. S. Aydil, J. Cryst. Growth **311**, 4188 (2009).
[67]O. Warschkow, Y. Wang, A. Subramanian, M. Asta, and L. D. Marks, Phys. Rev. Lett. **100**, 086102 (2008).
[68]J. L. F. Da Silva, C. Stampfl, and M. Scheffler, Surf. Sci. **600**, 703 (2006).
[69]W. R. Tyson and W. A. Miller, Surf. Sci. **62**, 267 (1977).
[70]The 1/3-ML alloy phase is discussed and ruled out as a stable surface phase in Sec. III E. Regarding the "Cu_3O_2" phase proposed in Ref. 18, we tested all stacking sequences $O^X_{2/3}Cu^YZn^AO^B\cdots$ in a $(\sqrt{3} \times \sqrt{3})$R30° unit cell with X and Y permuted over sites A, B, and C. The preferred stacking is $X = A$ and $Y = C$ (i.e., oxygen at the top and Cu at the fcc site) which, in fact, relaxes such as to position the Cu^C atomic plane above the O^A plane. This structure may alternatively be described as variant of our Cu_4O_3-ZnO(0001) phase containing a 1/3-ML oxygen vacancies. The stacking proposed in Ref. 18, namely, $X = C$ and $Y = B$, is 0.34 eV/(1 × 1) less stable. Neither of these two stackings is thermodynamically stable anywhere in our phase diagram.
[71]K. Akimoto, S. Ishizuka, M. Yanagita, Y. Nawa, G. K. Paul, and T. Sakurai, Solar Energy **80**, 715 (2006).